EXTENDING INTERFEROMETRIC SYNTHETIC APERTURE RADAR MEASUREMENTS FROM ONE TO TWO DIMENSIONS

A DISSERTATION
SUBMITTED TO THE DEPARTMENT OF GEOPHYSICS
AND THE COMMITTEE ON GRADUATE STUDIES
OF STANFORD UNIVERSITY
IN PARTIAL FULFILLMENT OF THE REQUIREMENTS
FOR THE DEGREE OF
DOCTOR OF PHILOSOPHY

Noah Bechor
December 2006

I certify that I have read this dissertation and that, in my opinion, it is fully adequate in scope and quality as a dissertation for the degree of Doctor of Philosophy.

Howard A. Zebker Principal Adviser

I certify that I have read this dissertation and that, in my opinion, it is fully adequate in scope and quality as a dissertation for the degree of Doctor of Philosophy.

Norm Sleep

I certify that I have read this dissertation and that, in my opinion, it is fully adequate in scope and quality as a dissertation for the degree of Doctor of Philosophy.

Roland Burgmann
(Department of Earth and Planetary Science
University of California, Berkeley)

Approved for the University Committee on Graduate Studies.

Abstract

Interferometric synthetic aperture radar (InSAR), a very effective technique for measuring crustal deformation, provides measurements in only one dimension, along the radar line of sight. Imaging radar measurements from satellite-based systems are sensitive to both vertical and across-track displacements, but insensitive to along-track displacement. Multiple observations can resolve the first two components, but the along-track component remains elusive. The best existing method to obtain the along-track displacement involves pixel-level azimuth cross-correlation. The measurements are quite coarse (typically 15 cm precision), and they require large computation times. In contrast, across-track and vertical InSAR measurements can reach centimeter-level precision and are readily derived.

We present a new method to extract along-track displacements from InSAR data. The new method, multiple aperture InSAR (MAI), is based on split-beam processing of InSAR data to create forward- and backward-looking interferograms. The phase difference between the two modified interferograms provides the along-track displacement component. Thus, from each conventional InSAR pair we extract two components of the displacement vector: one along the line of sight, the other in the along-track direction. Multiple MAI observations, either at two look angles or from the ascending and descending radar passes, then yield the three-dimensional displacement field.

We analyze precision of our method by comparing our solution to GPS and offset-derived along-track displacements from interferograms of the M7.1 1999, Hector Mine earthquake. The RMS error between GPS displacements and our results ranges from 5 to 8.8cm. Our method is consistent with along-track displacements derived by

pixel-offsets, themselves limited to 12-15cm precision. The theoretical MAI precision depends on SNR and coherence. For SNR=100 the expected precision is 3, 11cm for coherence of 0.8, 0.4, respectively.

Finally, we evaluate how the new measurements improve the determination of the earthquake coseismic slip distribution by comparison of models derived from multiple data types. We find that MAI data help constrain the southern portion of the lip distribution, by adding information where GPS data are sparse and the deformation is below the azimuth pixel-offsets detection threshold.

Acknowledgments

First and foremost I would like to thank my advisor, Howard Zebker, for clear and honest guidance. I've learned from him both through direct advice and through learning by example.

I would also like to thank my committee, Roland Burgmann and Norm Slip, for helpful discussions and thoughtful reviews. Each of them contributed to the success of this work.

Special thanks are due to Anthony Frazer-Smith, Adina Paytan and Shimon Wdowinski, for encouragement and advice, as well as much appreciated discussions.

Thanks are also due to the radar interferometry group and graduates, especially: Fayaz Onn, Sang-Ho Yun, Shadi Oveisgharan, Ana Bertran-Ortiz, Lauren Wye, Pyiush Shanker Agram, Leif Harcke, Jorn Hoffmann and Andy Hooper, for InSAR-related and none-InSAR related discussions, and for those so important and helpful coffee breaks and over-the fountain discussions.

To the Packard 3rd floor lunch group (including but not limited to): Sarah, Herfna, Kerry, Cecil, Kamakchi...

I would like to thank my family and friends in Israel, David, Tamar and Orit, for their encouragement, and new friends, especially Jing, Richard and Chris, for their humor and understanding, and for all the things I've learned from them.

And, almost last but not least, I would like to thank Yuval, for being there for his wife through graduate school.

This work was supported by the School of Earth Sciences in Stanford University. Data were acquired by the European Space Agency and made available through the WinSAR consortium.

Contents

List of Tables

List of Figures

Chapter 1

Introduction

Over the past two decades interferometric synthetic aperture radar (InSAR) has become a widely used tool for measuring surface displacements. InSAR provides surface displacement maps of 5 to 20 meter resolution, with centimeter-level precision. The technique, which gives nearly global coverage and is free of ground surveys, has allowed researchers to study previously inaccessible regions. Each displacement map is a one-dimensional projection of the three dimensional surface displacement field along the satellite line of sight (LOS). InSAR has several limitations: sparse temporal coverage, reduced signal to noise ratio over vegetated and snow-covered areas, atmospheric noise, and the one-dimensional measurement. The first three limitations are addressed in new satellite and instrument designs, however the fourth is difficult to address with hardware design changes. In this work we show that it is possible to derive two-dimensional, rather than one-dimensional, displacement maps from a single interferogram, and that this capability adds significantly to our ability to model surface deformation processes.

Surface displacement measurements provide information about crustal processes and upper mantle rheology. They have been widely used to study the seismic cycle, volcanoes and other tectonic-related processes as well as non-tectonic processes, such as slow landslides, glacier flow, post-glacial rebound, ground water-level changes, drilling-related subsidence, and underground nuclear experiments. Here we focus on displacements associated with the seismic cycle, however the methods developed can be used for studying many other processes.

There are several requirements for useful measurement of surface displacements associated with the seismic cycle. The first would be spatial and temporal coverage, as earthquakes occur in both expected (e.g., known faults along plate boundaries [*Wald et al.*, 1991; *Bear et al.*, 1999; *Langbein et al.*, 2005; *Johanson et al.*, 2006]) and unexpected (e.g. previously unmapped faults, [Hauksson et al., 1995; Price and Sandwell, 1998; Bodin and Hoeton, 2004) locations, and on occurrence intervals varying from seconds to hundreds of years and more. The great advantage of InSAR measurement is global coverage, currently with roughly monthly sampling rate. The type of processes we address here have spatial scales of several meters to hundreds of kilometers; of these, we can only study those that can be adequately sampled with time scales of months. This effectively excludes seismic waves, however it includes many cumulative types of displacements: coseismic, postseismic, some transients and interseismic. These processes produce surface displacements ranging in magnitude from several millimeters to meters.

The second requirement for measurement of surface displacements associated with the seismic cycle is precision. The precision of a single interferogram may vary from one centimeter to several meters. It is possible to reach sub-centimeter precision when the displacement accumulation rate is large enough to allow for repeated sampling, where the use of time-series InSAR provides better signal to noise separation [e.g., *Burgmann and Schmidt*, 2000; *Ferretti et al.*, 2001; *Lyons and Sandwell*, 2003; *Hooper et al., 2004*].

The third requirement is three dimensional observations, which we discuss in this work. Tectonic systems display various orientations, and produce surface displacements in all directions. The displacements vary with the tectonic setting, type of faulting, and the process(es) that generate the displacement. InSAR's one-dimensional measurements are oriented in a limited set of directions defined by the satellite orbit. The polar orbital configuration used by most remote-sensing satellites provides two such measurements, one when the satellite travels north to south, the other when the satellite returns from south to north. With the exception of near polar observations, the two displacement projections are mainly sensitive to the vertical and east (or west) displacement components. Systems whose major principle direction is close to

north-south orientation, or whose north-south displacement components are particularly informing, are difficult to study with InSAR. Examples include the San Andreas Fault system and the Dead Sea Fault, among others.

1.1 Contributions

In this thesis we extract an additional displacement projection map from each InSAR pair, with centimeter level precision. The new projection is oriented perpendicular to InSAR's prescribed measurement direction, therefore adding information in InSAR's least sensitive direction. In those cases where two projections are already available, our technique provides the necessary information to span the full 3D space. The scientific contribution of this work can be divided into three categories. First is the method contribution for crustal deformation studies using space geodesy and InSAR. The new technique extends the type and scope of work that can be done with InSAR: the surface displacement field can be obtained with no ground-based observations. This is particularly useful in areas where InSAR is the only available geodetic measurement. Second is the geophysical contribution to studies of the Hector Mine earthquake, through our improved models. Third are the broader-scale contributions: the technological advance can and probably will be used by engineers designing the next generation of satellites, enabling measurement of such phenomena as ocean waves, currents, and atmospheric water vapor changes.

1.2 Thesis Road Map

The questions we answer here are: Can we span the full 3D surface displacement field with currently operating InSAR satellites? To what precision? How are models improved by the new data?

In chapter 2 we provide background material about the InSAR technique, and define the concepts that are used later in the thesis.

In chapter 3 we examine why we need more than one or two components of the

surface deformation field. We identify the displacement components InSAR measurements are least sensitive to, and define the 'missing component'. We also provide an overview of the methods currently in use to compensate for the lack of information.

In chapter 4 we present a new measurement technique, which provides InSAR's missing component. We test the method's performance on the Hector Mine earthquake co-seismic deformation field and compare the results to previous studies. We also quantify the method's theoretical performance, and find that for the currently operating ERS and Envisat systems the method's expected precision ranges from 3 to 11 cm. This chapter was published *Geophysical Research Letters* in June this year [*Bechor and Zebker*, 2006].

In chapter 5 we apply the method to further study the Hector Mine earthquake. We examine the method's contribution by comparing the inferred slip distribution with: (1) GPS displacements, (2) MAI+InSAR+GPS measurements, and (3) previously published InSAR+GPS+azimuth pixel offset displacements. We examine the solutions in light of two separate model roughness criteria. We find that while the new data provide some improvement in the predicted surface rupture, the main features of the slip distribution and fit to data are already available in the GPS-based inversion.

In chapter 6 we summarize the thesis findings and conclusions.

Chapter 2

InSAR Background

In this chapter we provide background information on synthetic aperture radar (SAR) and interferometric SAR (InSAR), and define the parameters used later in this thesis.

Based on interfering repeated acquisitions of SAR images, InSAR provides one-dimensional surface displacement maps. InSAR was first developed in the 1970s [*Richman*, 1971; *Zisk*, 1972], and was first applied in the 1980s for topographic mapping [*Zebker and Goldstein*, 1986; *Gabriel and Goldstein*, 1989] and remote sensing of ocean currents [*Goldstein and Zebker*, 1987; *Goldstein et al.*, 1989]. The first deformation applications appeared in the 1990s [*Massonet et al.*, 1993; *Zebker et al.*, 1994], and have been followed by numerous deformation studies since.

2.1 SAR

SAR imaging provides fine resolution radar images of the ground. The technique has many civil and military uses, including monitoring land use, deforestation and urban development, as well as scientific applications, such as monitoring ocean waves and ocean surface wind velocities, and surface deformation via interferometry.

SAR imaging consists of illuminating the surface with a moving antenna transmitting a stream of pulses. Each pulse illuminates an area on the ground called the antenna footprint, as illustrated in Figure 2-1. The imaging geometry includes the flight direction, which determines the along-track, or *azimuth* imaging axis, and the

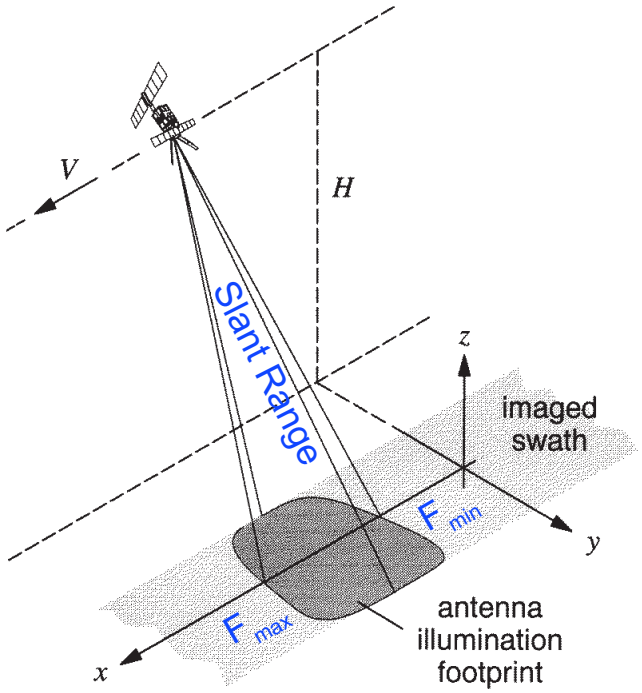

Figure 2-1: Illustration of SAR imaging geometry, modified from *Bamler and Hartl*, 1998. The antenna illumination footprint represents the area each pulse covers on the ground. $F_{\min}$ and $F_{\max}$ represent the Doppler frequency change due to the antenna's velocity in the along-track (x) direction. The returns from the antenna footprint have modified frequencies according to their relative location with respect to the antenna. This allows for sub-footprint resolution of half the antenna length, and for the beam steering used in this work.

range from the antenna to each spot on the ground, termed *slant range*, which defines the second imaging axis (Figure 3.1). As the antenna moves, successive pulses illuminate nearly overlapping areas on the ground. This provides repeating 'looks', or observations, of each spot on the ground. For the currently operating ERS and Envisat satellites, each spot is viewed by about 1200 pulses; the resolution of these systems is $5m \times 7.5m$ in the azimuth and slant range directions, respectively.

Fine SAR resolution is achieved via signal processing. To separate returns from sub-footprint locations, the technique takes advantage of frequency variations in the returned signals due to the Doppler effect in the along-track direction, and in pre-programmed pulse frequency modulation in the slant range. The many different

ways for integrating the SAR returns all incorporate the difference in time scales between the along-track and slant-range directions. In the along-track direction the governing speed is the antenna velocity; in the slant-range direction the governing speed is the speed of light. The two directions are therefore treated as nearly mutually independent in the processing. The returns are processed first in one direction, then in the other.

The processed ('focused') SAR image yields both amplitude and phase values for each pixel. In the next section we discuss SAR interferometry, or InSAR, which displays the phase difference between two SAR acquisitions covering the same area on the ground.

2.2 InSAR

InSAR methods yield the phase difference between two (or more) SAR acquisitions, and the phase difference is related to the change in distance from the satellite to the imaged area. Since its first topographic applications in the 1980's [*Zebker and Goldstein*, 1986; *Gabriel and Goldstein*, 1989], InSAR has been used for monitoring ocean currents [*Goldstein and Zebker*, 1987; *Goldstein et al.*, 1989] and slower movements, such as surface deformation due to tectonic processes [*Massonet et al.*, 1993; *Zebker et al.*, 1994; see also tables 1.1, 1.2 and 1.3 in chapter 1], glacier-flow [*Gray et al.*, 1998; *Eldhuset et al.*, 2003; *Forster and Jezek*, 2003], and slow landslides [*Nagler et al.*, 2002; *Hilley et al.*, 2004]. In this work we focus on interferometry for surface displacement measurements, where InSAR's centimeter-level precision depends on terrain properties and atmospheric conditions (see below).

InSAR involves 'interfering' two or more SAR images of the same area on the ground, acquired with different configurations and/or times. In Figure 3.2 we illustrate relevant InSAR parameters. The phase difference is measured along the satellite line of sight (LOS) of the reference (or master) SAR image. It is defined as the line from the antenna to the imaged element on the ground (Figure 3.2), and is similar in concept to the SAR slant range vector (Figure 3.1). In the first satellite pass (SAR1) the SAR antenna views a particular area on the ground in angle θ_1. In the second

pass (SAR2) the same spot is viewed from a slightly different angle θ_2. The view angle difference $\Delta\theta$ can be expressed also in terms of distance between the satellite positions at the two acquisition times. The *baseline* is defined as the physical distance between the two antennas (B in Figure 3.2). The distance from the satellite position in the master acquisition to the LOS of the slave acquisition is the *perpendicular baseline*, illustrated as $B_\perp$ in Figure 2-2. The difference in viewing angle $\Delta\theta$ is also shown in Figure 2-2.

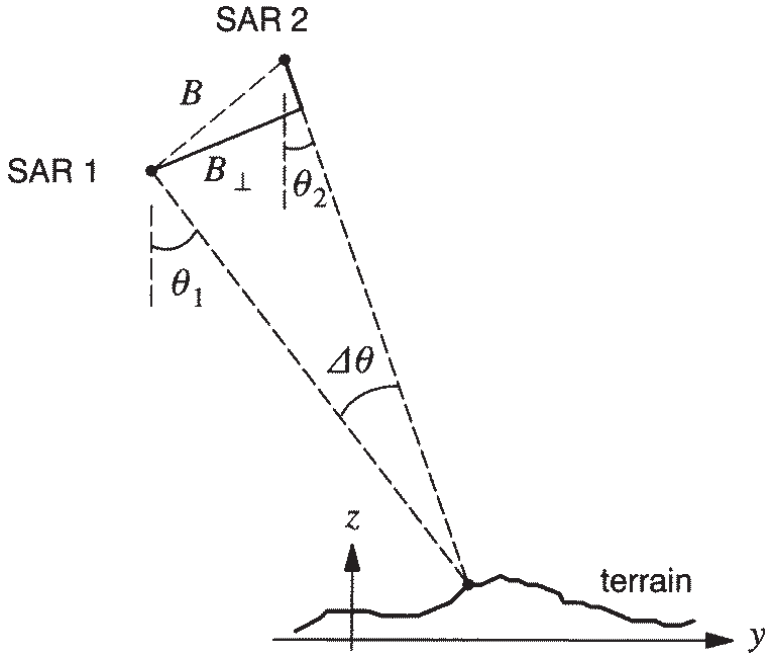

Figure 2-2: Illustration of InSAR baseline, modified from *Bamler and Hartl*, 1998. The flight direction is perpendicular to the paper plane. The baseline is defined as the distance B between the antenna position at the first and second passes. Alternatively, it can be expressed as the angle between the two viewing directions $\Delta\theta$, proportional to the perpendicular baseline $B_\perp$. This is a determining factor for coherence and topographic mapping, as discussed below.

Phase measurement noise is usefully addressed with the interferometric *correlation*. The correlation is a measure of how the interferometric phase relates to interaction with the scatterers on the ground [*Zebker and Villasenor*, 1992]. It is a unitless number ranging from 0 to 1, with 0 meaning no correlation and 1 meaning perfect correlation. The interferometric correlation of a pixel i is defined as follows:

$$\rho_i = \frac{\boldsymbol{E}[M_i \cdot S_i^*]}{\sqrt{\boldsymbol{E}[M_i \cdot M_i^*]\boldsymbol{E}[S_i \cdot S_i^*]}} \tag{2.1}$$

where $\boldsymbol{E}[\cdot]$ is the expectation of the quantity inside the square brackets, and M_i, S_i are the pixel's complex values in the master and slave images, respectively. To evaluate a given interferogram's correlation, we typically average several adjacent pixels in order to estimate their expectation.

Each process that modifies the interferometric phase may also affect the correlation. The different contributions to the InSAR phase can be divided into spatial and temporal effects:

- Spatial factors. We refer to all the phase changes that appear when there is a difference in viewing geometry of the first and second satellite passes (Figure 2-2) as spatial factors. These include topography, scale, rotation and transformation changes between the two SAR images, and spatial decorrelation.

- We use the term temporal variations to refer to all the phase changes that result from the passage of time between the two SAR acquisitions. These include deformation, travel-path variations, system noise, and temporal decorrelation.

Once the data are corrected for topography, the remaining interferometric phase variations are related to range-changes according to [*Zebker et al.*, 1994]:

$$\Phi = \frac{4\pi}{\lambda}\Delta r_i \tag{2.2}$$

where Δr_i represents the slant range change to range bin i, and λ is the radar wavelength. The angular representation of range change means the results are mod 2π, also known as *wrapped* phase. We use the two-dimensional phase unwrapping algorithm by *Chen and Zebker* [2002], commonly known by its coded name, snaphu, to unwrap the interferogram.

As we have seen, the InSAR distance measurement for a single interferogram takes place along a line connecting the antenna and the imaged pixel. This line is commonly referred to as LOS, and is sometimes called slant range. In the next

chapter we examine why InSAR's one-dimensional measurements are insufficient for observing certain displacement fields, and define the question that we later answer in this work.

Chapter 3

The Need for Centimeter-level 3-Dimensional Global Surface Displacement Maps

In this chapter we define InSAR's missing component, explain why adding this component is necessary, and describe different approaches currently in use to overcome the lack of information.

3.1 The Problem

Crustal deformation occurs at many different locations on the globe, and at various temporal and spatial scales. If we wish to monitor and study the many processes leading to crustal deformation, we need accordingly flexible measurement tools. Interferometric Synthetic Aperture Radar (InSAR) provides global repeat coverage, which allows for monitoring surface displacements at centimeter to tens of centimeter level precision and over 5m to 100km spatial scales [*Zebker et al.*, 1994; *Bamler et al.,* 1998]. InSAR's unprecedented resolution and coverage provides scientists with a much needed tool, which has lead to several otherwise impossible discoveries [e.g., *Peltzer et al.,* 1996; *Fielding et al.,* 2004; *Hilley et al.,* 2004; *Fialko et al.,* 2005; *Fialko et al.,* 2006]. However, InSAR measurements of crustal deformation have so far been limited to one to two components of the three-dimensional surface displacement field.

Crustal deformation processes lead to three-dimensional surface displacement fields, thus InSAR's limitation means lack of information. This information is particularly needed, for example, where the major principal direction of the geophysical system in question is parallel to InSAR's missing component (see below), where source geometry asymmetries play an important role in forming the observed displacement field, and when more than one process contributes to the surface displacement field (see the 'Need For 3-D Measurements' section below for more details). While for displacements on the order of tens of centimeters and greater other solutions exist (see 'Previous Solutions' section below), we lack these data for displacements on the order of a few cm and below, including most inter- and postseismic displacements. There now exist several approaches to overcome this limitation, and several proposed new satellite designs, which, if implemented, could provide measurements of the missing component [*Wright et al.*, 2004; *Wadge et al.*, 2003; Echo proposals to NASA]. The proposed satellite designs, however, present technical challenges, that remain unresolved. As a result no such satellite is planned in the foreseeable future. Further, we would like to be able to extract this information from existing satellite data.

Obtaining InSAR's 'missing component' is the fundamental problem we set out to solve in this thesis.

3.1.1 InSAR's Missing Component

InSAR is a 1-dimensional imaging technique, which provides the phase difference between repeated SAR acquisitions of the same spot on the ground. The phase difference is related to the change in distance from the antenna to the spot, along the satellite line of sight (LOS, Figure 2.1). Each pixel in the InSAR interferogram provides information on the displacement projection along the LOS.

In Figure 3-1 we illustrate the SAR imaging geometry. In the currently employed European Space Agency InSAR satellites, ERS and Envisat, the LOS is oriented nearly perpendicular to the satellite flight direction, looking to the right. The satellite along-track direction is termed azimuth, and the direction created by the projection of the LOS on the ground is termed range. A typical ERS interferogram covers a 100

km by 100 km area, and the antenna look angle (Figure 3-1), or the angle of the LOS with the vertical, varies from 20^o to 26^o across the range. Because the measurements are oriented along the LOS, InSAR measurements are insensitive to displacements along the direction perpendicular to the plane created by the LOS and the vertical.

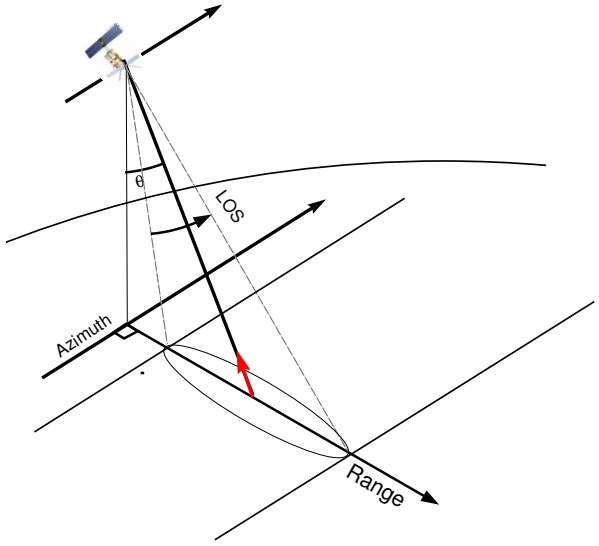

Figure 3-1: Illustration of imaging geometry. Each pixel in the single SAR image represents phase and intensity returns from the corresponding spot on the ground. To obtain displacements, a second satellite pass at a later time provides a similar image. The phase difference between the two images is related to the displacement projected along the satellite line of sight (LOS), illustrated as a red arrow. The angle θ is the antenna look angle. In ERS satellites θ ranges from 20^o to 26^o.

Current InSAR satellites are installed in polar orbits, which provide two viewing angles of the same spot on the ground: one view angle when the satellite travels from the South pole to the North pole (ascending orbit), and a second view angle in the other direction (descending orbit). In Figure 3-2 we illustrate the corresponding InSAR displacement vectors. The orbit configuration allows for two projections of the surface displacement field. Together, they span the vertical displacement component and a linear combination of the horizontal components.

The new InSAR satellite Envisat has the capability to image the same area on the ground from several different look angles, as illustrated in Figure 3-3. The radar antenna, however, is fixed with respect to the satellite. As a result, the different LOS

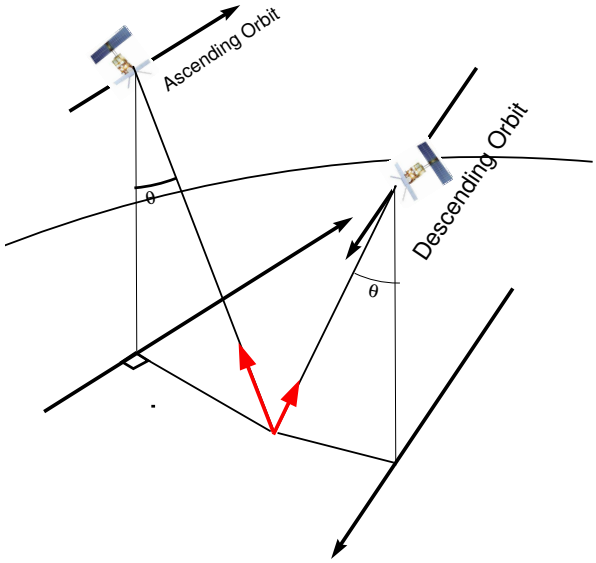

Figure 3-2: InSAR displacement vectors. The currently operating InSAR satellites are deployed in polar orbits. A given area on the ground may be viewed from both the ascending and descending orbits, providing altogether two length-change maps, each containing 1D projections of the 3D surface displacement field.

measurements have nearly identical range (i.e. horizontal) orientation in each of the ascending and descending orbits (Figure 2.3). The new capabilities, while allowing for denser temporal sampling, do not provide enough information to separate the two horizontal surface displacement components [*Wright et al.*, 2004].

The LOS of currently operating InSAR satellite antennas is oriented in a plane perpendicular to the satellite flight direction ('azimuth' direction), with slight variations. As a result the displacements obtained, projected along the LOS, are least sensitive to movements in the along-track direction. The additional information necessary in order to span the full 3-dimensional surface displacement field can therefore be provided by measurements in the along-track (azimuth) direction.

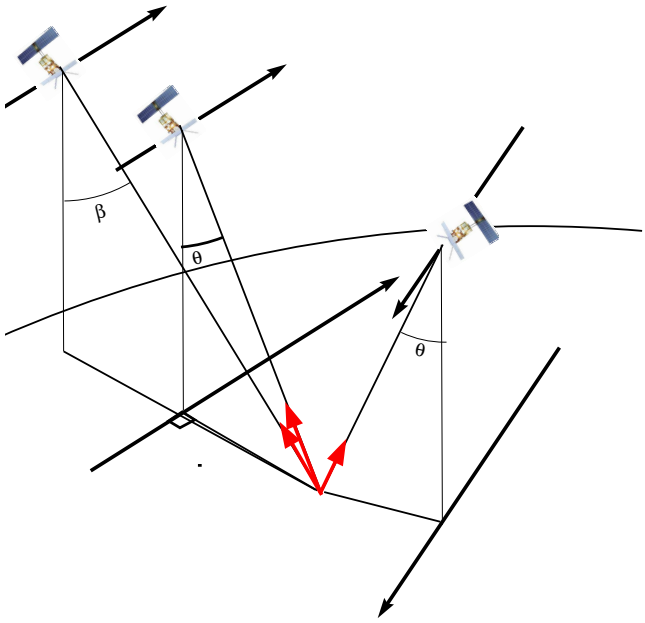

Figure 3-3: Illustration of InSAR displacement vectors with different look angles. The new InSAR satellite Envisat Advanced SAR instrument can image the same area on the Earth surface from different look angles, denoted by angles θ and β in the figure.

3.2 Need For 3-D Measurements

While the importance of adding a new component of deformation to the observed field may seem obvious, some benefits of the added information are worth highlighting. In some cases, most of the deformation produced is oriented along the satellite flight direction, and this component of deformation simply cannot be measured. One example of this is the Parkfield segment of San Andreas fault, where the interseismic strain accumulation rate in the conventional InSAR measurement direction is lower than 1 cm/year [*Johanson et al.*, 2006]. In other cases, separation of the two horizontal displacement components provides clues to the physical process(es) or geometry of the deformation source. We provide some examples in this section.

The Parkfield section of the San Andreas Fault (SAF) is a good example of where the fault orientation and major principle displacement direction disfavor InSAR measurements. In Figure 3-4 we present the interseismic GPS site velocities in Parkfield [*Murray et al.,* 2001], and the along-track satellite path. The InSAR measurement

orientation is perpendicular to the along-track direction, and the displacement rates are mainly horizontal. As a result (Figure 3-4), the displacement rate projections along the LOS are up to 1 cm/year. In inter-seismic measurements, researchers increase the SNR by averaging (or stacking) of repeated measurements, or by using more sophisticated time-series analysis methods [*Ferretti et al.*, 2001; Hooper et al., 2004]. In Parkfield, however, the combination of low LOS displacement projections and high decorrelation rates makes InSAR deformation measurements a challenge.

Another benefit of 3-dimensional imaging accrues when several processes occur simultaneously to produce the surface displacement field. For example, *Burgmann et al.* [2006] used horizontal GPS measurement and InSAR LOS changes to separate tectonic and non-tectonic vertical displacement sources, including landslides, long-term ground-water level changes, and sediment settling. Non-tectonic deformation sources may be active in conjunction with tectonic processes in other regions or areas. However, dense GPS networks are not available globally, and 3-dimensional observations were absolutely necessary to separate contributions from tectonic and non-tectonic processes [*Burgmann et al.*, 2006].

3.3 Previous Solutions to the Missing Component Problem

The missing deformation components are needed to use the InSAR measurements effectively. This information may come from three sources: (1) assumptions about the source, such as expectations of how the observed deformation should appear (several references are provided in Table 3.1), (2) augmentation of the InSAR measurements with independent measurements, such as GPS displacements (see Table 3.2 for several published studies using this approach), and (3) for cases in which the displacements are larger than $\sim 15cm$, cross correlations of the pixel power in the corresponding SAR images to provide the horizontal components (see Table 3.3). In most cases, all available information sources have been used.

In the next chapter we present a new technique to solve the same problem. We

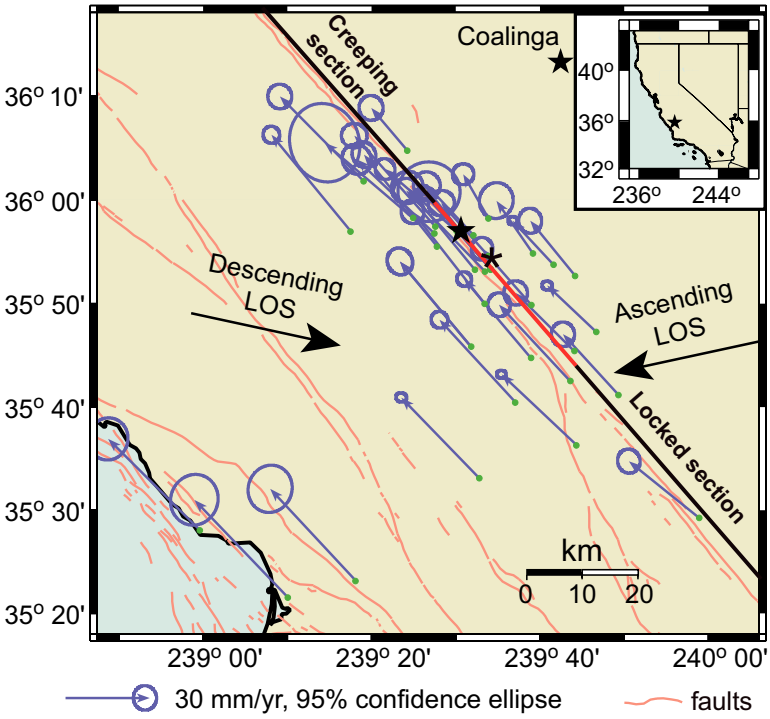

Figure 3-4: Interseismic GPS site velocities in the Parkfield section of the San Andreas Fault, after *Murray et al.*, 2001. Inset: location map. Arrows denote horizontal displacement rates with 95% confidence error ellipses. Black arrows illustrate the satellite along-track direction in the ascending and descending orbits. The measured LOS changes are nearly perpendicular to the along-track direction, resulting in less than centimeter/year change projected along the LOS. Movement along the creeping section of the fault was imaged with InSAR; however, the orientation of the interseismic velocity field along the creeping-to-locked transition zone of the fault (red line) results in LOS changes that are less than the measurement noise in that area.

Reference	Region and Event(s) or seismic cycle phase
Funning et al., 2005	1998 Aiquile earthquake, Bolivia, coseismic
Cakir et al., 2006	2004 Al Hoceima earthquake, Morocco, coseismic
Catita et al., 2005	1998 Pico-Faial earthquake, Azores, coseismic
Crippa et al., 2005	1997 Umbria-Marche earthquake sequence, Italy, coseismic
Hsu and Burgmann, 2006	Longitudinal Valley Fault, Taiwan, interseismic
Wright et al., 2003	2002 Nenana Mountain earthquake, Alaska, coseismic
Jacobs et al, 2002	1999 Hector Mine earthquake, California, coseismic

Table 3.1: Example InSAR publications

Reference	Region and Event(s) or seismic cycle phase
Chileh et al., 2004	North Chile Subduction Zone, all phases of seismic cycle
Johanson and Burgmann, 2005	SAF Northern Transition Zone, interseismic creep and earthquakes
Wright et al., 2004	2002 Denali earthquake, Alaska
Burgmann et al., 2002	1999 Duzce earthquake, Turkey
Pederson et al., 2003	Two 2000 South Iceland earthquakes
Arnadottir et al., 2003	Two 2000 South Iceland earthquakes
Fialko, 2004	1992 Landers, California earthquake
Pritchard et al., 2002	1995 Antofagasta earthquake, Chile
Burgmann et al., 2006	San Francisco Bay Area, interseismic
Cakir et al., 2005	North Anatolian Fault, Turkey, interseismic
Lyons et al., 2003	Southern SAF, California, interseismic
Peltzer et al., 2001	Eastern California Shear Zone, transients
Peltzer et al., 1998	1992 Landers earthquake, California, postseismic
Wright et al., 2004	Major faults, Western Tibet, interseismic

Table 3.2: Example InSAR/GPS publications

Reference	Region or Event
Fielding et al., 2005	2003 Bam earthquake, Iran
Fialko, 2004	1992 Landers earthquake, California
Sandwell et al., 2002	1999 Hector Mine earthquake, California
Fialko et al., 2001	1999 Hector Mine earthquake, California
Peltzer, 1999	1997 Manyi earthquake, Tibet
Peltzer and Rosen, 1995	1993 Eureka Valley earthquake, California

Table 3.3: Example InSAR/Pixel offsets publications

compare it to the results obtained for the M7.1 1999, California Hector Mine earthquake by *Agnew et al.* [2002] and *Fialko et al.*, [2001].

Chapter 4

Measuring 2-Dimensional Movements Using a Single InSAR Pair

In the previous chapter we discussed the importance of measuring the full 3-D surface displacement field.

Here we present our new approach to measure the along-track surface deformation component with InSAR. We begin by describing the new method, and examine its theoretical precision. We then apply the new method the co-seismic displacements due to the Hector Mine earthquake, and compare the results to GPS observations of the same surface displacements by *Agnew et al.* [2001], and to pixel-offset displacements by *Fialko et al.* [2001].

4.1 Summary

We present a new method to extract along-track displacements from InSAR data. The new method is based on split-beam processing of the InSAR data to create forward- and backward-looking interferograms. The phase difference between the two modified interferograms provides the along-track displacement component. Thus, from each conventional InSAR pair we extract two components of the displacement vector: one along the line of sight, the other in the along-track direction.

We analyze the new method's precision by comparing our solution to GPS and offset-derived along-track displacements in interferograms of the 1999, Hector Mine

earthquake. The rms error between GPS displacements and our results ranges from 5 to 8.8 cm. Our method is consistent with along-track displacements derived by pixel-offsets, which are limited to 12-15 cm precision.

The theoretical precision of the new method depends on SNR and coherence. For SNR=30 the expected precision is 3, 11cm for coherence of 0.8, 0.4, respectively.

4.2 Introduction

A major limitation of InSAR for geophysical applications is that the technique is only sensitive to one-dimensional motion along the satellite's line of sight (LOS), while most deformation is better characterized using three dimensional geodetic data. Thus, many studies have incorporated multiple radar passes using different geometries to resolve off LOS motions [e.g. *Funning et al.*, 2005; *Fialko*, 2004; *Froger et al.*, 2004; *Joughin et al.*, 1998]. Although these solutions typically provide some separation between spatial deformation components, they cannot span the full 3D space accurately with data acquired by currently operating satellites. A satellite with both left and right looking capability in a non-polar orbit is necessary to fully resolve three-dimensional deformation using conventional InSAR [*Wright et al.*, 2004]. Such satellite designs have been proposed [*Wadge et al.*, 2003, *Echo proposals to NASA*], however their construction offers technical challenges, and these systems are thus expensive. As a result, no left- and right-looking satellite mission is planned for the foreseeable future.

If existing satellites are operated to obtain both ascending and descending radar passes over a single area, two components of deformation may be inferred from the interferogram phases. The third component may be inferred from pixel amplitude offset analysis [*Michel et al.*, 1999a,b], albeit at very reduced sensitivity. In this approach two or more amplitude images are cross correlated piecewise, to obtain a strain image. This method is in fairly wide use [e.g.*Fialko et al.*, 2005; *Simons et al.*, 2002; *Jonsson et al.*, 2001, *Fialko et al.*, 2001; *Peltzer et al.*, 1999;]. Studies comparing the amplitude pixel offset analysis with ground truth (GPS data) suggest the method's precision for ERS data with high correlation is limited to $\sim$ 12-15cm

[*Jonsson et al.*, 2001; *Fialko et al.*, 2001; *Fialko*, 2004]. Because cross-correlation accuracy depends on the size of the correlation windows, there is a trade-off between sensitivity and measurement density.

We present here a split-beam method, which we denote multiple aperture InSAR (MAI), that is both more efficient and a more accurate measurement of the along-track deformation component than pixel amplitude correlation. When applied to InSAR data acquired over the Hector Mine earthquake, we were able to increase precision by a factor of at least 2 over the results published by *Jonsson et al.* [2002] and *Fialko et al.* [2001]. While there is still a choice between measurement density and accuracy, the new method offers an improvement in precision with significantly reduced computation time.

4.3 Method

We measure the along-track component of deformation using sub-aperture processing in the along-track direction, thereby constructing forward- and backward-looking interferograms of the ground. The phase difference from the two look directions is proportional to any along-track deformation.

In the forward looking interferogram, the phase corresponds to changes along a LOS slightly forward of the nominal radar squint direction θ_{SQ} (Figure 4-1). Similarly, the backward-looking interferogram corresponds to deformation along a slightly different LOS. Subtracting the phases produces a phase difference representative of azimuth displacements between radar passes.

Consider a radar sensor with geometry as depicted in Figure 4-1. Denote the radar nominal 'squint' angle as θ_{SQ}, and the antenna angular beamwidth by α. To form the forward looking interferogram, we use only the forward part of the antenna beamwidth, and integrate around a new squint angle, $\theta_{SQ}+\beta$. For simplicity, consider integrating over one half beamwidth, so $\beta = \frac{\alpha}{4}$. The backward looking interferogram is similarly formed from the back half of the antenna beam. For a displacement x in

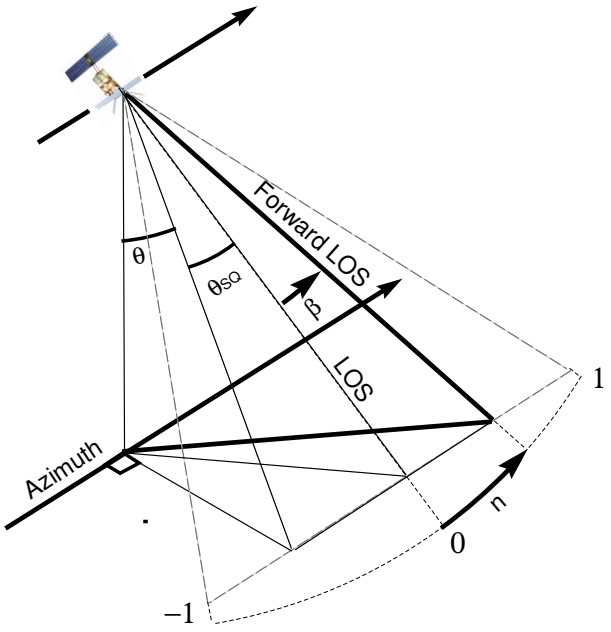

Figure 4-1: Illustration of MAI imaging geometry. The antenna mid-beam line of sight (LOS) has a 'squint' angle θ_{SQ}. We squint it further by an angle $\pm\beta$, to form forward- and backward-looking interferograms. The angle β is defined as a fraction n of half the beamwidth. The new along-track resolution is $\frac{l}{2(1-n)}$.

the along track direction, the interferogram phases Φ are:

$$\Phi_{\text{forward}} = -\frac{4\pi x}{\lambda} \sin\left(\theta_{\text{SQ}} + \frac{\alpha}{4}\right) \tag{4.1}$$

$$\Phi_{\text{back}} = -\frac{4\pi x}{\lambda} \sin\left(\theta_{\text{SQ}} - \frac{\alpha}{4}\right) \tag{4.2}$$

$$\Phi_{\text{MAI}} = \Phi_{\text{forward}} - \Phi_{\text{back}} = -\frac{4\pi x}{\lambda} 2 \sin\frac{\alpha}{4} \cos\theta_{\text{SQ}} \tag{4.3}$$

where λ denotes wavelength. For small α and θ_{SQ}, $\Phi_{\text{MAI}} = \frac{2\pi x}{\lambda}\alpha$. Since $\alpha \approx \frac{\lambda}{l}$, where l is the antenna length:

$$\Phi_{\text{MAI}} = \frac{2\pi}{l} x \tag{4.4}$$

For the ERS satellite $l = 10$m, and 1m of along-track displacement yields about 0.6 radians of phase difference.

Inverting and expressing the results in terms of uncertainties,

$$\sigma_x = \frac{l}{2\pi} \sigma_\Phi \tag{4.5}$$

where σ_Φ and σ_x are the standard deviation of the phase and displacement measurements, respectively.

For an interferogram with a given signal to noise ratio (SNR) and effective number of looks N_L, the phase noise can be approximated by [*Rodriguez and Martin*, 1992]:

$$\begin{aligned} \sigma_\Phi &\approx \frac{1}{\sqrt{2N_L}} \frac{\sqrt{1-\rho^2}}{\rho} \\ \rho &= \frac{\mid \rho_{\text{spatial,temporal}} \mid}{1 + \frac{1}{\text{SNR}}} \end{aligned} \tag{4.6}$$

where the total correlation ρ includes decorrelation sources as defined in *Zebker and Villasenor* [1992].

We note that it is possible to generate the forward- and backward-looking interferograms using only a portion of the available beamwidth, thereby generating a split aperture wider than $\frac{\alpha}{2}$. To formulate the forward/backward squint β as a function of antenna angular beamwidth α, we define a normalized squint $n = \frac{2\beta}{\alpha}$, shown in

Figure 4-1. Changing the aperture width has two opposing effects: increasing the phase sensitivity to deformation and reducing the SNR. The SNR decreases because the total along-track integration time decreases. As a result the optimal aperture width is different for different SNR and correlation values. Because the resolution degrades with aperture loss, the effective number of looks is also reduced.

Figures 4-2(a-c) show the theoretical standard deviation of the along-track displacement measurement as a function of normalized squint n for ERS, with various SNR and correlation values. Results for SNR = 316, 31 and 3, with correlation $\rho = 0.2$ to $\rho = 0.8$ are displayed in figures 4-3a, b and c, respectively. We note that for SNR= 3 the optimal squint is $n = 0.5$, increasing to 0.6 for ten times higher SNR, and to 0.666 for SNR= 316. We assume averaging over 32x32 pixel windows. This number refers to pixel averaging and not effective looks: we account for resolution reduction with aperture widening by calculating the effective number of looks to produce Figure 4-2.

Because the topographic phase contribution is not very sensitive to squint direction, its contribution to the interferometric phase appears in both interferograms. Similarly, the cross-track and vertical components of deformation contributions to phase are identical in the forward and backward looking interferograms. In addition, because the angular beamwidth is ~ 0.3 degrees for ERS, and the atmospheric water vapor is concentrated below $1-2$ km height, the forward- and backward-looking LOS pass through similar lower atmosphere. Specifically, any delay due to atmospheric water vapor variations of wavelength larger than ~ 5 meters is will also be present in both interferograms, assuming that water vapor is concentrated in the first 1 km of the troposphere. Therefore phase contributions from these factors cancel in the differential interferogram, leaving only the along-track displacement term.

The new technique therefore provides the along-track component directly. MAI can be applied to other InSAR systems, such as RADARSAT, JERS, Envisat and ALOS.

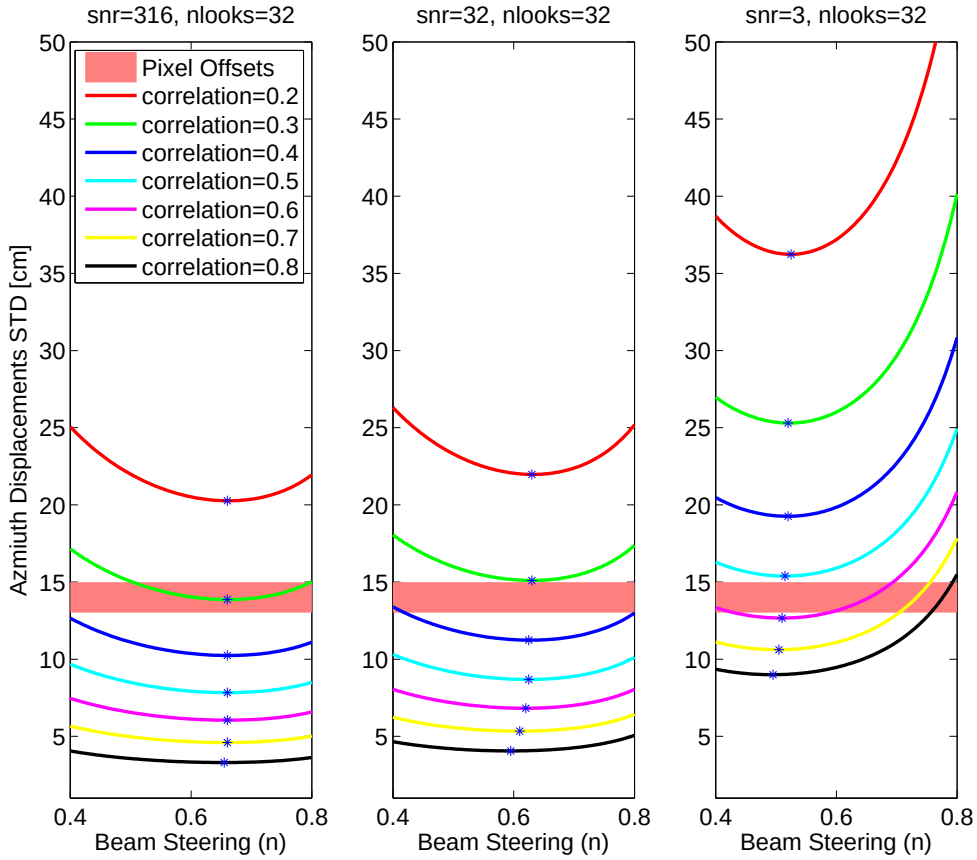

Figure 4-2: Predicted standard deviation variations. Curves are derived from *Rodriguez and Martin* [1992] and equation 5. We present theoretical precision for correlation values of 0.1 to 0.8, as a function of antenna beam widening n (see text and Figure 1). Results are shown for three SNR orders of magnitude and 1024 looks; typical ERS SNR ranges from 10 to 100 over land. Published range for pixel-offset analysis is denoted as a pink line, using values from *Jonsson et al.* 2001.

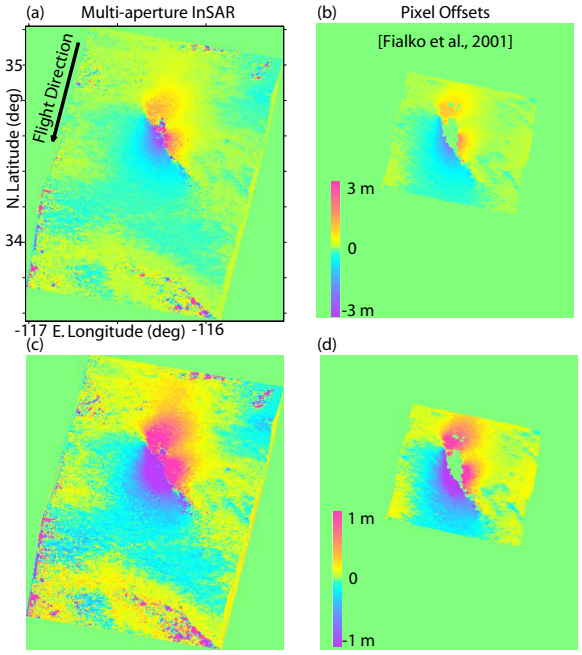

Figure 4-3: MAI displacements, and comparison to AZO displacements. All subfigures cover the same area. (a),(b) MAI and pixel-offset [Fialko et al., 2001] displacements for the Hector Mine earthquake earthquake. Displacements are in the along-track direction, which is denoted by a black arrow. (c),(d) same as top figures, with scale $\pm$1m.

4.4 Application

We applied our method to InSAR analysis of the Mw 7.1 1999 California, Hector Mine earthquake, because GPS and offset-derived displacements are available [*Agnew et al.*, 2001; *Jonsson et al.*, 2001; *Fialko et al.*, 2001]. We used the descending orbits pair of 23027, September 15, 1999 and 23528, October 20, 1999, track 127, frame 2907, both acquired by the ERS-2 satellite, with perpendicular baseline of $21m$.

We implement the MAI algorithm using conventional InSAR software (range-Doppler processing), steering the beam by modifying the Doppler centroid f_{DC}, and limiting the integration time to the appropriate interval. We estimate a minimum SNR of 76 from comparing brightness in different parts of the conventionally processed SAR images, and therefore use a beam-widening of $n = 0.6$, and 0.4 times the total integration time. The modified Doppler centroids are $f_M = f_{DC} \pm n \cdot \frac{v}{l}$, where v is

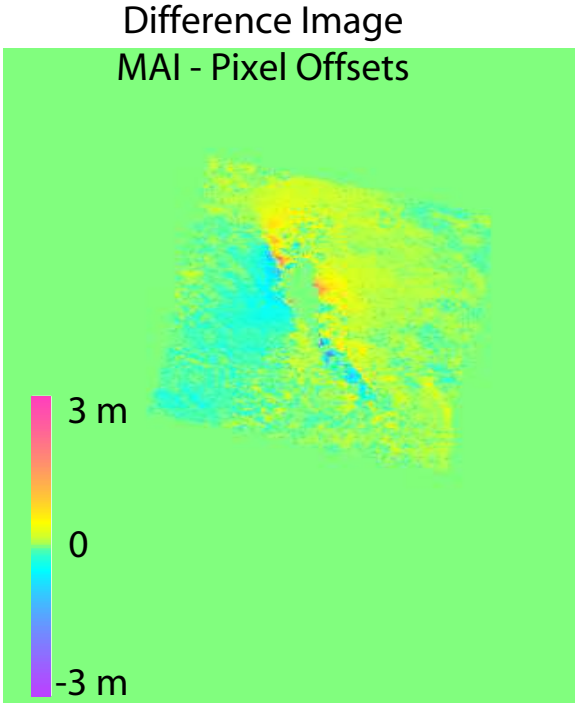

Figure 4-4: Difference plot of MAI minus AZO measurements. The rms of the difference between the two measurements is 22.6cm.

the effective velocity of the satellite. To map the MAI phase changes to along-track displacements we account for the change in LOS direction across the swath.

The results (Figure 4-3a) show a similar pattern to the pixel offset analysis displacements from *Fialko et al.* [2001] (Figure 4-3b). To better visualize the differences we also plot the displacements using a color scale of ± 1 (Figure 4-3c,d). Note that MAI shows a larger spatial extent of deformation. Note in Figure 4-3d that the pixel-offset result shows a value of $\sim$ 10 cm in the far-field. In order to plot the difference between the two results we first subtract this value from the pixel-offset result, and then calculate the difference (Figure 4-4). The MAI algorithm yields larger absolute displacement values than the azimuth offset calculation in all but the south-west deformation side-lobe. The rms of the the difference between the two measurements is 22.6 cm.

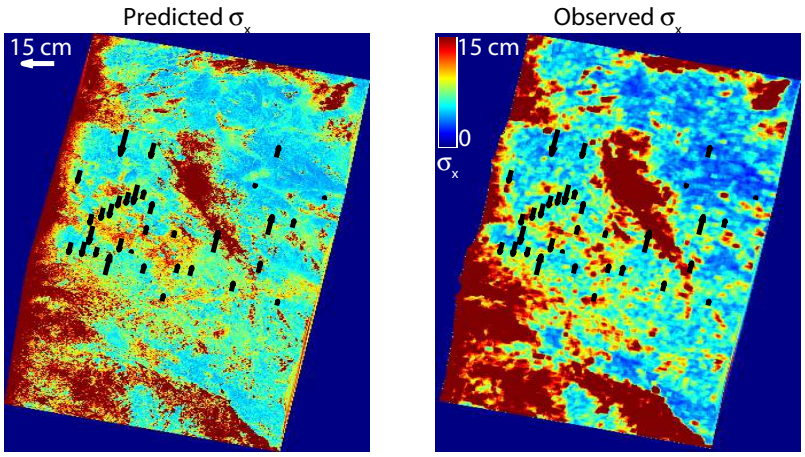

Figure 4-5: Theoretical (left) and observed (right) precision of the new method. Arrows denote difference between GPS and MAI, plotted in the along-track direction. The predicted σ_x was calculated from the InSAR coherence image and equation 5, and a lower bound on SNR. We obtained a minimum SNR estimate of 76 from the power ratio between a dark and a bright area in the SAR images. The predicted σ_x therefore represents an upper bound. The observed σ_x is calculated over 10x10 pixel windows. The map appears to have a coarser resolution due to the windowing effect. Note that in some parts of the image the observed σ_x betters the theoretical bound, likely due to SNR variations .

We calculate the expected error in the MAI displacements using equation 5, modified for $n = 0.6$, equation 6, and the measured interferogram coherence. The theoretical standard deviation map (Figure 4-5, left panel) agrees with the experimentally measured standard deviation of displacements (Figure 4-5, right panel) within 8 cm. The observed precision betters the theoretical limit in some areas likely because we used a lower bound on the SNR. In areas with high coherence (> 0.8), measurement standard deviation ranges from 2 to 4 cm. A coherence of 0.6 corresponds to $\sim$ 8 cm. A coherence of 0.4 leads to $\sim$ 10 cm, and still lower coherence leads to $>$ 15 cm standard deviation.

We also compare the MAI displacements with GPS observations from *Agnew et al.* [2001], projected on the along-track direction. The GPS sites are distributed in areas with MAI precision of 5 to 24cm, therefore providing a way to test the accuracy of the new method in this range. In Figure 4-6 we present the predicted precision

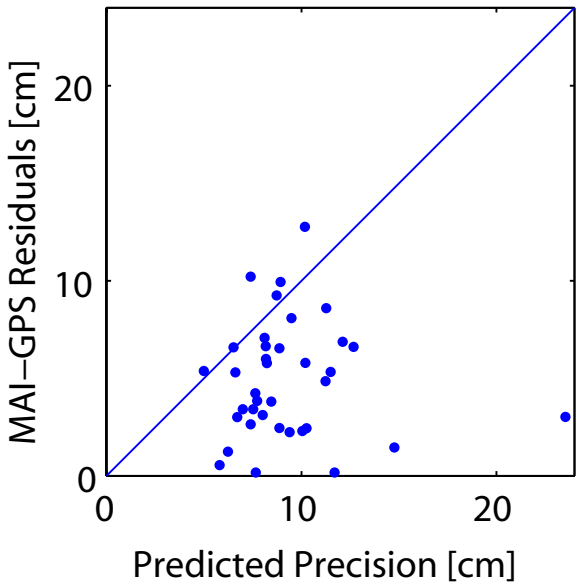

Figure 4-6: Predicted precision versus actual GPS-MAI residuals, for GPS data collected up to two months after the earthquake. The residuals equal or better the theoretical standard deviation for most GPS sites. The GPS-MAI residual for GPS site CHUK (not shown) is $-1.39m$, however the predicted error is $55cm$. The projected GPS displacement at CHUCK is $2.1m$. This discrepancy suggests an upper bound of $\leq 2m$ on the maximum deformation that can be measured with MAI.

plotted against the GPS-MAI residuals. For 84% of the GPS sites, the predicted precision is equal or better than the actual errors. We plot MAI displacements at the 68% confidence level against the GPS displacements in Figure 4-7a. The root mean square (rms) error between the GPS and the MAI displacements is 8.8 cm all GPS receivers, and the slope of the least-squares line fit between them is 1.

The InSAR and MAI interferograms represent cumulative displacements from the earthquake and 4 days of post seismic deformation. The GPS displacements, on the other hand, span different time periods, with about half the sites (30) including post-seismic deformation spanning 6 and 3 months after the earthquake, with up to 3cm displacements [*Agnew et al.*, 2001]. A better comparison is therefore to compare displacements taken at the same time. We compare in Figure 4-7b the MAI displacements with GPS displacements spanning the earthquake and up to two months after the earthquake. The rms error now drops to 6.9 cm. Tighter time constraints (2

weeks) can drop the rms error down to 5 cm, however then the best fit slope changes to 0.8, possibly due to bias caused by the location of the GPS sites. We estimate that the new method's precision for the Hector Mine earthquake is about 5.5-6.5 cm for the descending orbit pair.

In Figure 4-7c we display the GPS and MAI+InSAR vectors in a horizontal grid, with the new along-track horizontal vector oriented in its true direction, and the conventional LOS magnitude drawn perpendicular to it. We plot the GPS displacements corresponding to up to 2 months after the earthquake on the InSAR grid, projected into the same directions. We note the similarity in direction and magnitude. The 3-dimensional GPS displacements are projected to the LOS and along track directions; it is possible that large uncertainties in the GPS vertical may contribute to differences between InSAR and GPS displacements in the LOS direction. Because many of the GPS sites are located in areas of low coherence, we suspect that the precision derived from the MAI/GPS comparison may underestimate the performance of the new method.

4.5 Conclusions

Using the new technique, InSAR provides two displacement vectors per interferometric pair. Hence, InSAR, conventionally thought of as a 1-D measurement, in fact contains 2-D phase information that can be extracted using split-beam processing.

The new method, multiple aperture InSAR (MAI), reveals 2-D displacements per interferogram as applied to measurements of the 1999 Hector Mine earthquake coseismic deformation. The results are consistent with GPS displacements measured by *Agnew et al.* [2001], and agree qualitatively with the pixel offset analysis by *Fialko et al.* [2001]. The rms error between the GPS and MAI displacements ranges from 5 to 6.9 cm depending on the amount of post-seismic deformation included in the GPS but missing from the InSAR data.

We find that for interferogram coherence of 0.4 and higher, with SNR of 30 and higher, MAI out-performs the best-case precision expected from pixel-offset analysis.

MAI is easy to implement using conventional InSAR software, and is applicable

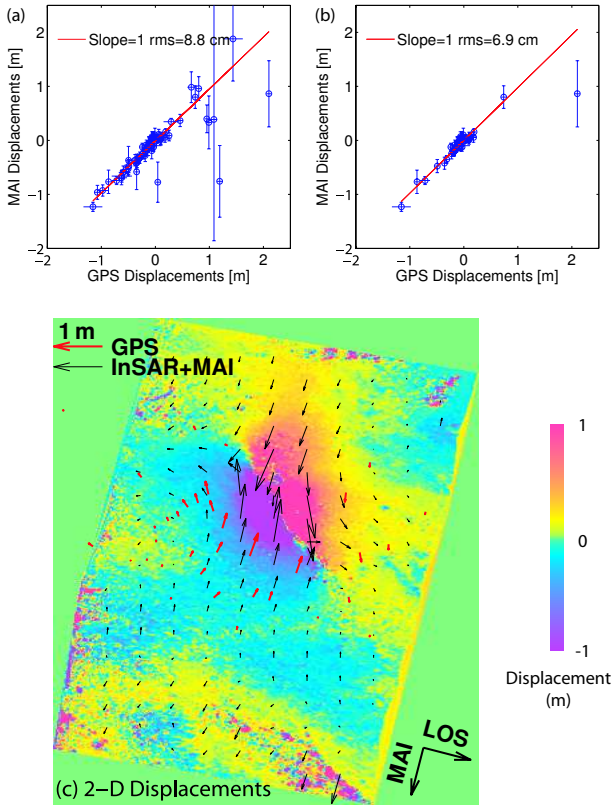

Figure 4-7: Comparison between MAI and GPS displacements. GPS displacements are from Agnew et al., 2001. In (a) and (b) GPS and MAI displacements are plotted in the horizontal and vertical axes, respectively. Circles with bars denote MAI displacements with error bars at 68% confidence level. The red line is the best-fit least squares line, whose slope is 1 in both figures. (a) Comparison using all 71 available GPS data in the imaged area, about 30 of which were gathered 6 months after the earthquake. The rms error is 8.8 cm and includes up to 3 cm of post-seismic displacements. This is significantly less than 15cm published by *Jonsson et al.*, 2001, and *Fialko et al.*, 2001 for both ascending and descending orbits. (b) Same comparison, using GPS sites that were operated up to 2 months after the earthquake. The rms error here is 6.9 cm, reduces to 6.3cm without the outlier, and may be still biased by some post-seismic deformation. (c) Vector-plot with InSAR LOS and MAI along-track displacements (black arrows) and GPS displacements up to 2 months after the earthquake (red arrows). Vector directions correspond to the along-track direction and LOS plotted in the perpendicular direction. Because the GPS displacements were projected to the LOS and along-track directions, the larger uncertainties in the GPS vertical displacements were propagated into the LOS projection, and may account for some of the variation in that direction.

to interferograms with along-track oriented displacements, such as ERS and Envisat observations along the San-Andreas fault system. Its increased precision over existing offset-derived along-track displacements makes it a useful tool for analyzing many deformation fields.

Chapter 5

Modeling With MAI

In the previous chapter we introduced a new method to obtain precise along-track displacements from InSAR data, using multiple-aperture InSAR (MAI), and demonstrated that MAI provides more accurate measurements than the previously available azimuth offsets measurements (AZO). In this chapter we examine how the new data improve slip-distribution models of the Hector Mine earthquake.

5.1 Approach

The question we ask in this chapter is: are slip distribution models of the Hector Mine earthquake improved by the new data? To address this question we compare three model solutions, each based on a different subset of the available geodetic data: (1) a GPS-based solution, (2) a solution based on all the available geodetic data except for the MAI data (GPS, InSAR and AZO), and (3) a similar solution with MAI replacing the AZO data.

We evaluate the use of the 2-D data by comparing the GPS-based solution with solutions including the InSAR and MAI data. This provides us with an understanding of the level of improvement one might expect from adding the radar-interferometry data: if the GPS-based model does a poor job of predicting the independent radar measurements, then we would expect to see a significantly different solution when the radar measurements are included in the inversion. If, on the other hand, the observed and predicted radar displacements are similar, we can infer that the GPS

displacements provide enough information to obtain the main features of the slip distribution. In this case we would expect the radar-based data to optimize the solution, but not to change it drastically.

We begin with a solution based on GPS, InSAR and AZO displacements, thus including all the geodetic measurements that were available prior to developing the MAI technique. We then replace the AZO displacements with MAI, and repeat the process. We contrast these two solutions with each other, and with independent field measurements of the earthquake surface rupture.

5.2 Data and Data Reduction

In this section we discuss the data, their accuracy, and the data-reduction methods we will use for the analysis.

In Figure 5.1 we display the horizontal GPS displacements used in this work [*Agnew et al.*, 2001 and *Burgmann et al.*, in preparation]. The 75 GPS sites we use cover an area that spans from roughly 100 km east of the fault to 150 km west of the fault, and from 150 km north to 150 km south of the fault. The site distribution is not centered on the fault, and there are fewer GPS sites on the north-east side of the fault trace (8 GPS sites overall). The mean spacing of the GPS sites is one site per 35 km.

The GPS data consist of both campaign and continuous sites [*Agnew et al.*, 2001; *Hudnut et al.*, 2001]. The two GPS data sets were revisited by *Burgmann et al.* [in preparation], who provide a combined set of coseismic displacements. These include 24 of the 27 campaign GPS sites that were surveyed up to 10 days after the earthquake, and 145 continuous GPS sites located up to 500 km from the fault. We restrict our model to use displacements from GPS sites within a distance of 150 km from the fault. Using data from larger distance may violate our model assumption of a homogeneous elastic half-space, as factors such as the change of rigidity with depth become more pronounced at larger distances [*Burgmann*, personal communication].

Formal errors in the GPS data range from up to 4.6 cm for the campaign sites to several mm for the continuous sites (gray ellipses in Figure 5.1). In addition to

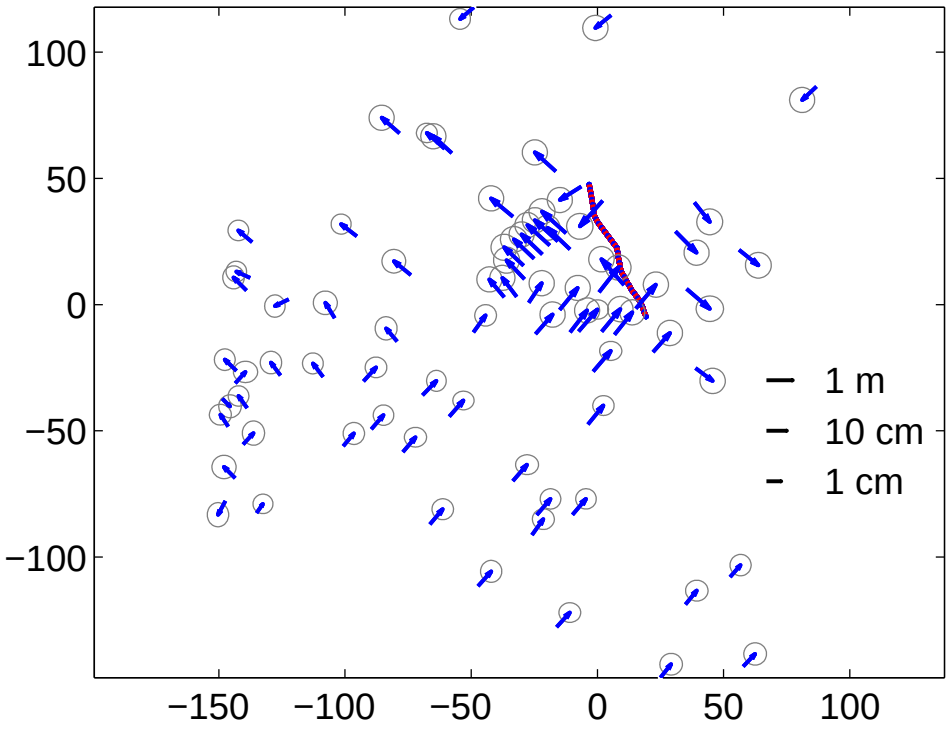

Figure 5-1: GPS displacements used in this study. The red line represents the modeled fault trace. GPS displacements (blue arrows) are displayed in logarithmic scale to avoid clatter. Three scale arrows (in black) show displacements in 1 m, 10 cm and 1 cm. The 95% confidence error ellipses are displayed in gray.

the formal errors, there can be systematic reference frame errors which may be different for the campaign and continuous GPS displacements, as the data were processed separately. Such a systematic trend, in the form of translation error, was found and removed from the displacements [*Burgmann et al.*, in preparation]. In addition, campaign GPS sites were surveyed at different epochs during a 7-year period before and 6 months after the earthquake, and therefore originally contained varying amounts of interseismic and post seismic displacements. A first-order estimate of these additional displacements was removed from the campaign GPS data by *Agnew et al.*, 2001. Imperfections in this estimate is another unaccounted-for source of error, which may be up to few cm [*Agnew et al.*, 2001].

The InSAR data used in this work comprise SAR images collected by the European Space Agency (ESA) ERS-2 satellite. We used the descending orbit pair of 23027 (September 15, 1999), and 23528 (October 20, 1999), track 127, frames 2907 and 2925, with a perpendicular baseline of 21 m. The LOS displacements from both frames are displayed in Figure 5.2. The data cover an area of 100 by 200 km, with the fault centered in the northern part of this area. The InSAR data present high resolution coverage, which may be important on the north-east side of the fault where there is are few GPS sites (8 sites overall, Figure 5.1). While the InSAR preferred resolution is $\sim$ 30 meters, we can only use a subset of these data in the modeling due to limited computer capacity. For modeling purposes we reduce the resolution to one point per 3 km, which is the highest data density consistent with our computing power (Figure 5.2, right panel). This reduced resolution is still an order of magnitude denser than the 34.5 km GPS resolution.

While formal error estimates for the InSAR measurements are available from the MAI algorithm, other error sources in InSAR measurements, including atmospheric noise, interferometric decorrelation, and reference frame (geocoding) errors, can corrupt the measurements. Of these, the easiest to quantify are decorrelation errors, as they have been formalized before and follow the interferogram correlation and SNR [*Rodriguez and Martin*, 1992; *Zebker and Villasenor*, 1992; also see Chapter 2 *InSAR Background*]. Atmospheric errors can be up to several centimeters, and may vary in scale from a pixel to a full interferogram. Geocoding errors appear in the form of image distortions. These do not modify the displacements, but do change the location of the displacements measuremetns. These errors may vary throughout the interferogram, and are potentially more pronounced in areas with high deformation gradients, such as hte area within several kilometers of the fault trace (Figure 5.2).

We use AZO displacements as determined by *Fialko et al.*, 2001 (Figure 5-3). The AZO displacements were obtained from the same SAR images; their spatial coverage is more restricted than the InSAR and MAI coverage (Figures 5-2, 5-4, respectively). While the InSAR and MAI cm-level sensitivity leads to visible signal also near the interferogram edges, the AZO 12 cm and more precision does not retrieve the smaller displacements.

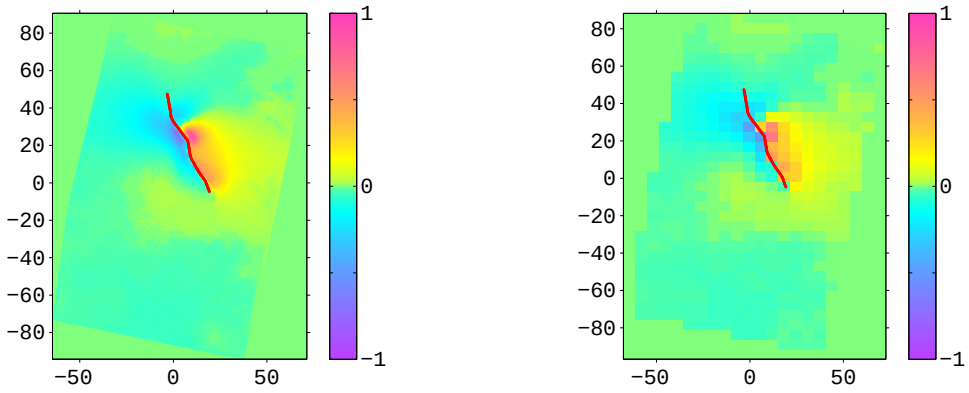

Figure 5-2: InSAR displacements used in this study. These are the LOS measurements, which are mainly sensitive to the vertical displacement component. The scale is ±1 m, one third of the maximum horizontal displacement (see below). The left side panel contains the interferogram in full (30 m) resolution; the right side panel contains the reduced-resolution image used in the modeling. The fault trace is plotted in red. Color scale is in meters.

Formal AZO errors are not available. The published AZO RMS error when compared with GPS displacements is 15 cm [*Jonsson et al.*, 2001]. Error sources include geocoding issues similar to the InSAR measurements, and reduced sensitivity in parts of the image were large deformation gradients do not allow for proper cross- correlation. These areas appear as green 'holes' in the AZO image.

We reduce the AZO data to the same 3 km resolution as the InSAR data in the modeling. While the calculation of the AZO displacements allows for 1.5 km resolution, we resample the data to 3 km to match the MAI reduced data set. We note that using 1.5 km resolution did not produce a visible change in the resulting solutions.

We use MAI displacements from the same interferometric InSAR pair [*Bechor and Zebker*, 2006], displayed in Figure 5-4. The MAI measurement covers the same area as the InSAR measurement, which is roughly twice that of the AZO displacements.

The MAI formal errors vary with interferometric correlation and SNR. In addition to the formal errors, geocoding errors may also affect the MAI precision. Similar to the InSAR image in Figure 5-2, the MAI displacements appear to miss the southern

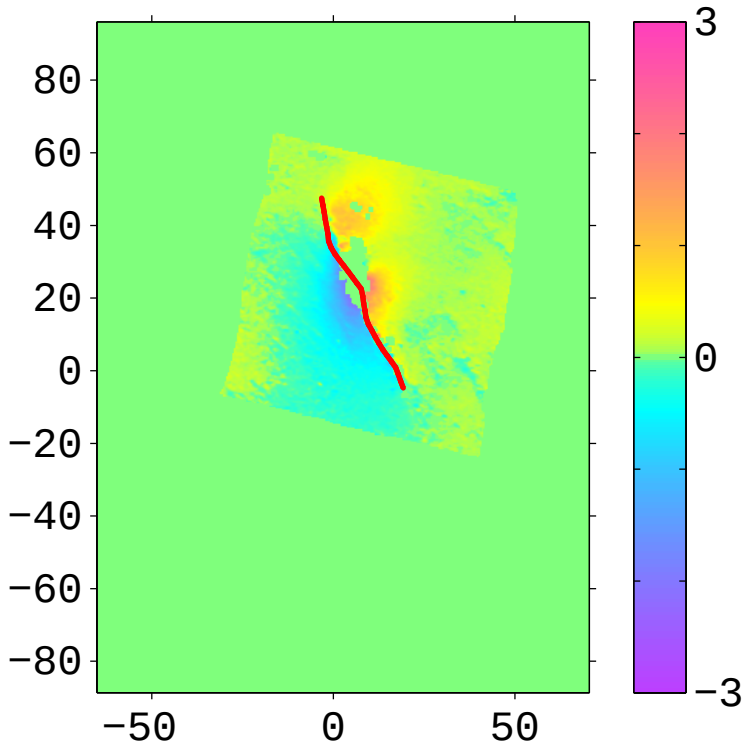

Figure 5-3: AZO displacements used in this study, after *Fialko et al.* [2001]. The fault trace is plotted in red; green spots next to the fault represent lack of measurement. Note the reduction in area covered when compared with the InSAR and MAI displacements in Figures 5-2 and 5-4, respectively. Color scale is in meters.

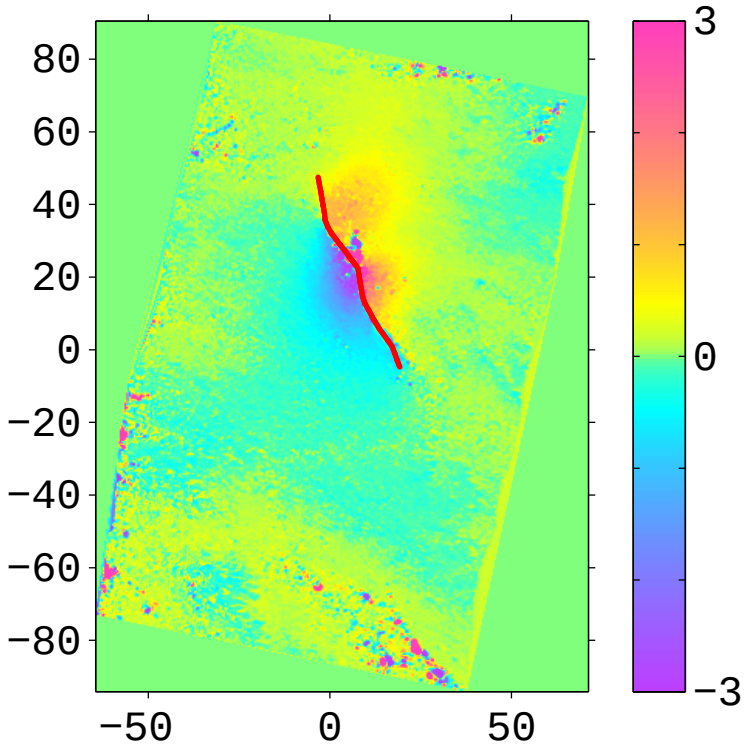

Figure 5-4: MAI displacements used in this study. Note the increase in covered area when compared with the AZO data in Figure 5-3. Color scale is in meters.

tip of the fault. We believe that this is due to a geocoding error, because the same error appears in both our InSAR and MAI images. It is missing from the AZO image, which was processed and geocoded elsewhere. Another reason for this disagreement might be a distributed-faulting area, which could have been missed by the AZO technique because of its lower precision.

We reduce the MAI data volume in the same way we reduced the InSAR and AZO displacements. All radar-based data was sampled at 3 km sampling for the modeling. While this spacing may seem low when compared with the original InSAR resolution of 5 to 100 m, the 3 km sampling is an order of magnitude better than the 35 km spacing of the GPS data.

5.3 Modeling Approach

In this section we describe the modeling approach for all three models. The material in this section includes the equations we use to model the data and constrain the solution, determination of constraint weighting, and data weighting used in the inversion.

5.3.1 Model Equations

We use inverse methods to determine the slip distribution from the various surface displacement measurements. We relate the surface displacements to slip using Green's functions for rectangular dislocations in a homogenous elastic half-space [*Okada*, 1992]. We assume the fault geometry of *Price and Burgmann* [2002], and solve for distributed slip by seeking a model m that minimizes the second norm $||\cdot||_2$ of the data-model residuals:

$$\Phi = ||W(d - Gm)||_2 \tag{5.1}$$

where G are the Green's functions, d are the surface displacement data, and W is the data weight matrix obtained from Cholesky factorization of the formal data covariance inverse $\Sigma_d^{-1} = W^T W$. The weighted system of equations is:

$$d_w = G_w m \tag{5.2}$$

where d_w and G_w are weighted data and Green's functions, respectively ($d_w = Wd$, $G_w = WG$).

Typically, solutions for slip using many small fault segments produce non-unique results. This happens because many different combinations of slip values fit the data equally well. Thus we apply constraints to limit the number of possible solutions. *Du et al.* [1992] suggested using nonnegativity and smoothing constraints, because a physical slip distribution is likely to have a uniform sign, and is not likely to contain sharp edges as the large stress variations are associated with non-tapering edges are not plausible for most rheological conditions. We apply nonnegativity using nonnegative least squares [*Lawson and Hanson*, 1974]. We use the Laplace operator as a

smoothing constraint, as suggested by *Du et al.* [1992]. The system of equations we solve is:

$$\begin{bmatrix} d_w \\ 0 \end{bmatrix} = \begin{bmatrix} G_w \\ \beta^2 \nabla^2 \end{bmatrix} m, \qquad \text{subject to} \quad m \geq 0 \tag{5.3}$$

where ∇^2 is the 2^{nd} order Laplace operator and β^2 is the relative weighting of the constraint with respect to the Green's functions. The zero-data are pseudo data associated with the smoothing kernel [*Du et al.*, 1992].

We add three more model parameters to account for orbit error in the radar data. Orbit error, a common source of error in InSAR, AZO and MAI displacements, affects the data mainly in the form of linear displacement gradients. We solve for a linear displacement gradient in each of the radar-derived solutions, together with the faulting equations to minimize this error.

5.3.2 Model Weighting

The smoothing constraint weighting, β^2, determines the relative weight of the data fit and solution smoothness in the inversion. Because β^2 depends on both the data weights W and the number of data available, slip distributions obtained using InSAR data require different β^2 values than similar solutions using GPS, AZO and/or MAI data [*Jonsson et al.*, 2002]. We therefore use a measure of the solution, rather than the data, to select β^2 values for the different data-type inversions. The model roughness, $||\nabla^2 m||_2$, provides a solution parameter that can be examined with respect to the data misfit in a trade-off curve (see Figures 5-5, 5-6, 5-7 for specific solution curves). We use such a trade-off curve to estimate β^2 for each model, following similar, previous works [*Du et al.*, 1992; *Jonsson et al.*, 2002]. We calculate the data misfit as the weighted residual root mean square (weighted RMS).

5.3.3 Data Weighting

In addition to the model internal weights, the solution also depends on the data weights. We use four different types of data in our solutions: GPS, InSAR, AZO and

MAI. Below we summarize the data weighting we assign to each data, as well as the data reduction approach we use for the high-resolution radar data.

While GPS, InSAR and MAI displacements are assigned formal errors for each data point [*Agnew et al.*, 2001; *Hudnut et al.*, 2001; *Bechor and Zebker*, 2006], the AZO data are not. We use the formal error estimates for the GPS, InSAR and MAI data.

We weight the InSAR LOS data following the MAI discussion of errors presented in the previous chapter. While MAI displacements are theoretically ~ 3 times noisier than the LOS displacements, we find that in practice their mean error is the same as the LOS RMS error when compared to the GPS data [8 cm, *Jonsson et al.*, 2002]. We expect the LOS and MAI variances to follow identical spatial patterns, as both depend on interferometric correlation and SNR. This does not apply to off diagonal terms in the covariance matrix, as the LOS displacements contain spatially correlated atmospheric noise and the MAI displacements do not. We note parenthetically that the LOS mean error of 8 cm, as determined from the RMS error with the GPS displacements, is 2 to 4 times higher than the maximum expected atmospheric noise in the area [*Onn and Zebker*, 2006]. We therefore assume that for our model comparison purposes the data variances we use adequately represent the LOS errors.

We weight the AZO data with uniform weights according to their reported RMS error when compared to the GPS data [15 cm, *Jonsson et al.*, 2002]. While we do expect some spatial variation in the AZO errors, we have no useful way of quantifying that.

Another data-handling issue is the reduction of geocoding error effects next to the fault trace. In Figures 5.2, 5.3 and 5.4 we display the radar-based data and overlay them with the modeled fault trace. We note that while most of the data show a marked discontinuity along the fault trace, as expected, both the LOS (Figure 5.2) and MAI (Figure 5.4) show a deviation of about 3 km between the observed and modeled fault trace along a 10 km strip in the southern portion of the fault. The AZO data, which were geocoded by *Fialko et al.*, 2001, show a deviation from the fault trace along a 10 km strip in the northern end of the fault trace. We attribute the similarity in the LOS and MAI observed location of the fault trace to the fact that they were

both geocoded in the same way; the AZO data were geocoded independently and therefore possibly contain different geocoding errors. We avoid the large effects that geocoding errors may have next to the fault by removing a 3 km-wide strip of data along the fault trace, as well as a wider, 6 km-wide strip along those fault segments which show obvious errors in the figures.

All three of the radar-based data types, LOS, AZO and MAI, are high resolution data containing thousands of data points. In order to reduce the amount of data into manageable size, we use one in every 30 data points. This reduces our resolution from 100 m to 3 km, which is still an order of magnitude denser than the average GPS resolution of one site per 35 km.

5.4 Model Solutions

In this section we describe the three solutions, their parameters and their ability to fit the different data sets. Table 5.1 contains a summary of the three solution parameters.

5.4.1 GPS-Based Solution

Our first solution is inferred using solely the GPS data. The slip distribution and trade-off curve are shown in Figure 5-5. The slip distribution's preferred roughness is 3.7, with maximum slip of 6.2 meters (see also Table 5.1).

The residuals between the GPS observed and predicted displacements (Figure 5-6) follow an arbitrary spatial pattern, and many of them are within the 95% confidence level of their formal errors. The weighted residual RMS is 3.2 mm, suggesting that we do fit most of the GPS data well in this solution.

A way to test the validity of a model is by examining its predictions for data that were not included in the solution. Specifically, the solution's prediction for the radar data can provide us with an idea of how well the surface displacement field was sampled with GPS in the first place. In Figure 5-7 we plot the residuals between the observed and predicted InSAR and MAI displacements (left and right panels,

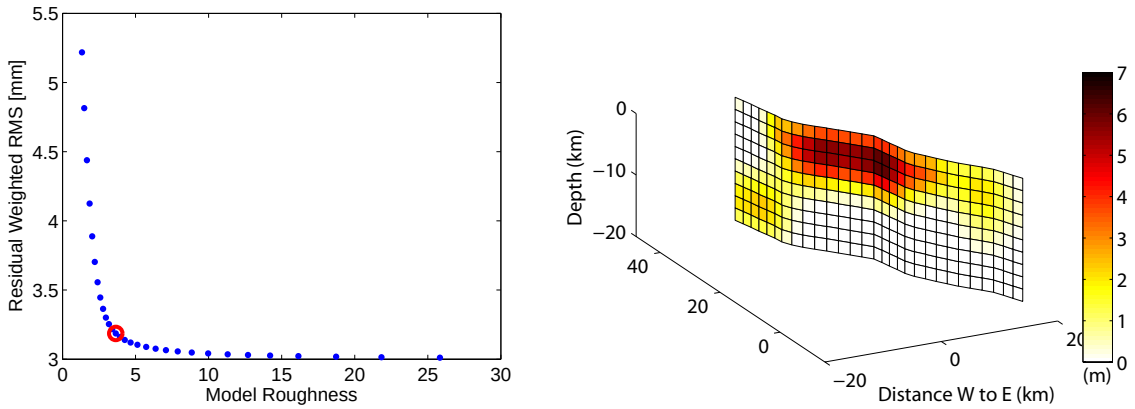

Figure 5-5: Solution based on solely the GPS data. The trade-off curve (left panel) was used for determining a preferred model smoothing β^2 of 0.004, which resulted in model roughness of 3.76. The slip distribution (right panel) has a maximum slip of 6.2 m. This solution already contains the major details necessary to predict the InSAR and MAI displacements (see text). Color scale is in meters.

respectively). Given that no radar-based data were used in inferring this solution, the data fit is visually remarkable. Quantitatively, the weighted residual RMS for the GPS, InSAR and MAI data is 1.8 mm, even though the InSAR and MAI data were not included in the solution. The residual standard deviation is 3.6 cm for the InSAR data and 19 cm for the MAI data. We therefore expect the radar-based data to slightly alter the slip distribution, however not to change it significantly.

5.4.2 GPS, InSAR and AZO-Based Solution

We next solve for slip distribution using all the geodetic data available without using the MAI technique. These include GPS, InSAR and AZO displacements. In Figure 5-8 we show the model roughness versus data misfit trade-off curve we used for choosing the preferred solution, and the preferred slip distribution. The slip distribution has roughness of 3.7, with a maximum slip of 6.3 meters (Table 5.1). Most of the slip is concentrated at first 10 km below the surface, with an additional slip concentration at 12 to 18 km. The largest slip values concentrate on a 2 by 4 km rectangle at mid-fault.

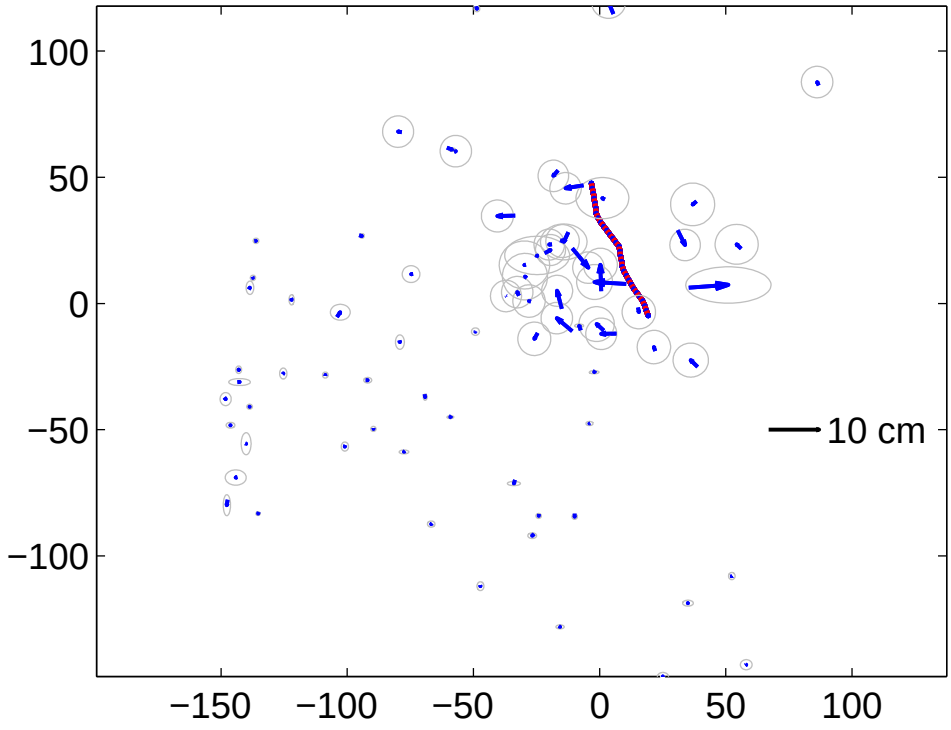

Figure 5-6: GPS displacement Residuals for the GPS-inferred solution. Most of the observed minus predicted displacements (blue arrows) are within the 95% confidence level error ellipses (gray ellipses). The largest residuals occur near the fault with the campaign GPS data. The weighted residual RMS is 3.2 mm.

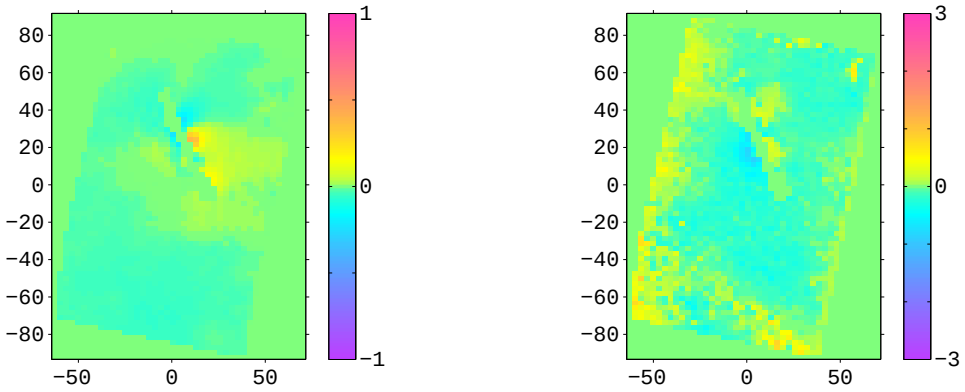

Figure 5-7: InSAR (left) and MAI (right) residuals for the GPS-inferred solution. The observed minus predicted residuals are plotted within the same range as the data (±1 m for InSAR LOS displacements and ±3 m for the MAI along-track displacements). Color scale is in meters.

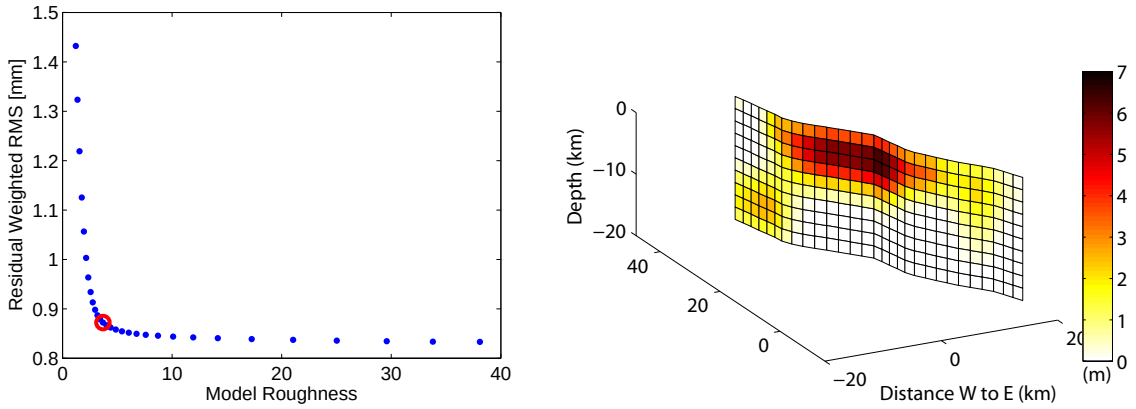

Figure 5-8: Solution based on all the available geodetic data without the new MAI results (that is, GPS, InSAR and AZO displacements). Maximum slip is 6.3 m, and weighted residual RMS is 0.8 mm (see text). Note the resemblance of this solution to the GPS-based solution in Figure 5-8.

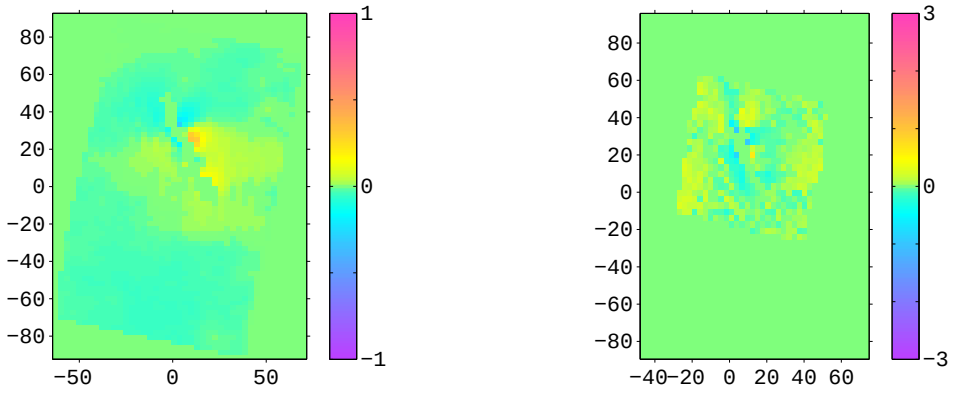

Figure 5-9: InSAR and AZO residuals, calculated from the data and the GPS, InSAR, and AZO-based solution. Color scale is in meters.

The weighted residual RMS for the GPS, InSAR and AZO-based solution is 0.8 mm. This number demonstrates that the assumed AZO data precision, of 15 cm, and does not represent an improvement in data fit. Because the AZO errors are 2 orders of magnitude larger than the GPS errors, any possible discrepancy between the AZO and GPS data is less than the AZO error.

We plot the residual patterns for completeness in Figure 5-9. Because the slight differences between the GPS-inferred and the GPS, InSAR and AZO-based solutions are in the uppermost 2 km of the fault we expect any improvements in fit to data to be located very close to the fault trace.

5.4.3 GPS, InSAR and MAI-Based Solution

Our third solution is based on the GPS, InSAR and MAI displacements. It is based on the same data as the previous solution, with the exception of the AZO data which are replaced with MAI displacements. In Figure 5-10 we display the preferred slip distribution and the trade-off curve we used for determining the model weighting. The preferred solution's roughness is again 3.7, with maximum slip of 6.7 m.

The residual weighted RMS for the GPS, InSAR and MAI-based solution is 1.6 mm, suggesting a slight improvement of 0.2 mm in fit to data, when compared to the GPS-based solution. Such slight improvement is well within the error of determining

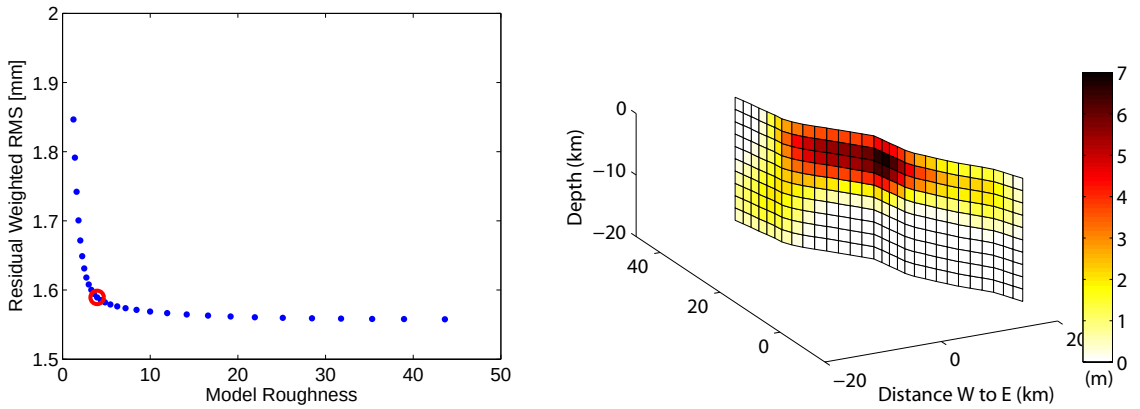

Figure 5-10: GPS, InSAR and MAI-based trade-off curve (left) and slip distribution (right). Color scale is in meters.

model roughness; however, since all the data combinations seem to require the same model roughness, it might suggest a real, however slight, improvement in data fit.

To check if the improvement in weighted residual RMS represents a change in data-fitting we plot the GPS residuals (Figure 5-11). Here we note that while east of the fault the residuals maintain the same pattern and magnitude as before (Figure 5-6), several residuals along the south-west portion of the fault changed magnitude and direction. The solution therefore represents a change in the distribution of errors, meaning that the MAI data are precise enough to affect the solution.

The standard deviation of the InSAR residuals is 3.4 cm, indicating that some of the improvement due to inclusion of the MAI data instead of AZO actually took place in the InSAR data fit (InSAR residuals are shown in Figure 5-12, left panel). The improvement in MAI residual standard deviation is 1 cm, from 19 cm for the GPS-based model to 18 cm in the current model. This is again an indication that the previously noted improvement was not accidental.

We expect a 1 cm improvement in data fit to be visible in the MAI residual plots. Compare the MAI residuals for the current solution (Figure 5-12, right panel) with the same information for the GPS-based solution (Figure 5-7, right panel). We note visible improvement on a 100 by 50 km area centered on the southern-most third of the fault.

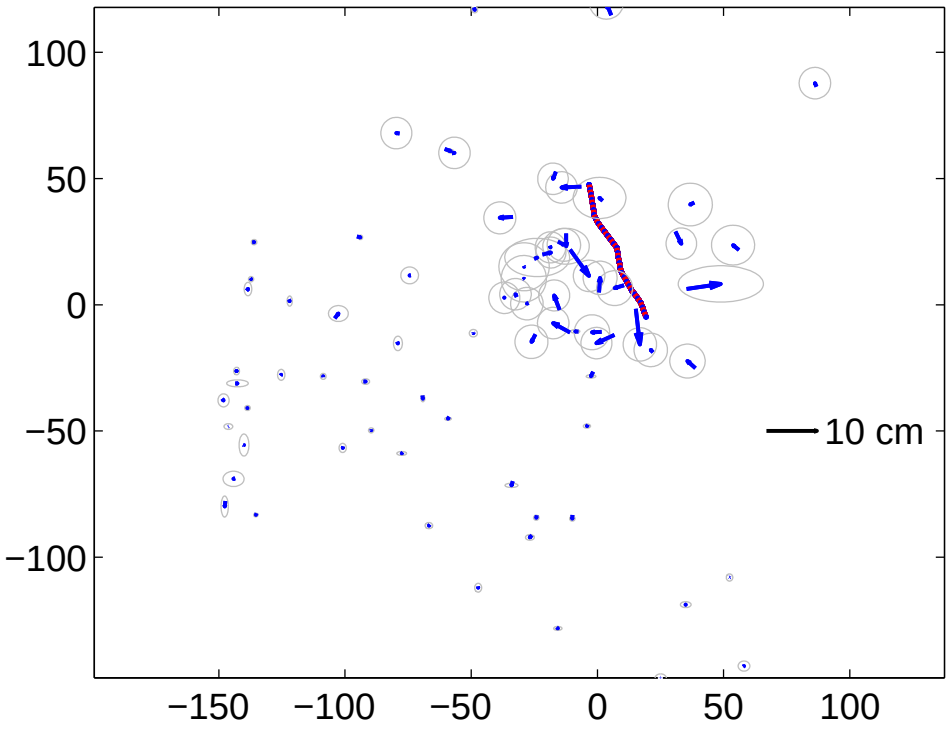

Figure 5-11: GPS residuals (blue arrows) calculated from the GPS data and their prediction by the GPS, InSAR and MAI based solution. Note the quadrant from 0 to 25 km to the south and west of the fault; this is where the residual pattern and magnitude is different from those of the GPS-only-based model in Figure 5-6.

Data	Maximum slip	β^2	Roughness	WRMS
GPS data	6.2 m	0.004	3.7	3.2 mm; 1.8 mm
Previous data (GPS, SAR, AZO)	6.3 m	0.0043	3.7	0.8 mm
Current data (GPS, SAR, MAI)	6.7 m	0.006	3.7	1.6 mm

Table 5.1: Summary of the three solution parameters. The GPS-based solution weighted residual RMS (WRMS) is 3.2 mm for the GPS data, and 1.8 mm for the GPS, InSAR and MAI data.

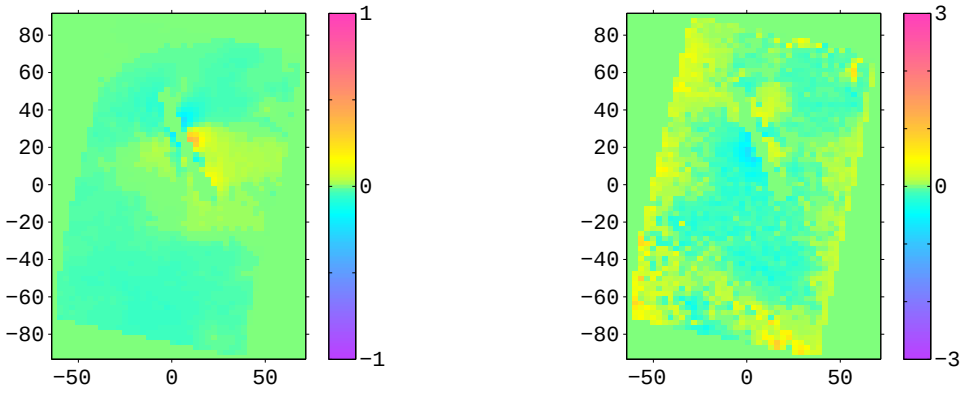

Figure 5-12: InSAR (left) and MAI (right) residuals calculated from the data and GPS, InSAR and MAI-based solution. Note the southern-most third part of the fault. The MAI data fit on this $\sim$ 100 by 50 km area is improved compared to Figure 5-7. Color scale is in meters.

5.5 Discussion and Conclusions

We investigated slip distribution models of the Hector Mine earthquake using three different types of available geodetic data. We find that GPS data provide sufficient information to explain the cruder details of the slip distribution, including solution roughness roughness (3.7) and depth ($\sim$ 10 km). Used by themselves, GPS data reasonably predict the InSAR data, via slip modeling, within 3.6 cm, and the MAI data within 19 cm accuracy.

A second solution, based on GPS, InSAR and AZO displacements is nearly identical to the GPS-based solution (Figure 5-13). As the InSAR data is already predicted by the GPS data within 3.6 cm, inclusion of LOS information in the inversion did not produce significant changes. This is partly because of the strike-slip faulting of the Hector Mine earthquake, in which horizontal displacements are more meaningful than vertical displacements. We note that the reported AZO precision of 15 cm [*Jonsson et al*, 2001; *Fialko et al.*, 2001] is nearly two orders of magnitude larger than the GPS precision. As a result, the AZO data add little useful information.

Our third solution is based on GPS, InSAR and MAI displacements. This solution includes the same GPS and InSAR data as the previous solution, however we replaced

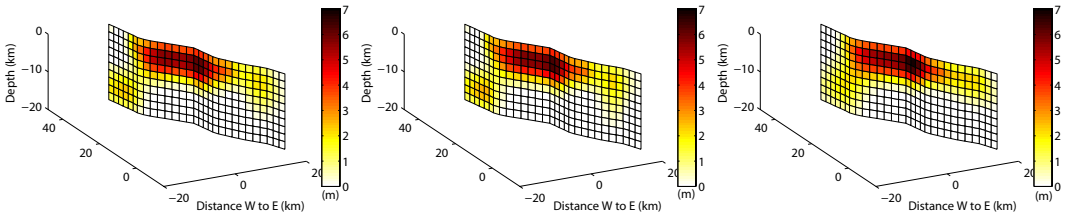

Figure 5-13: Comparison of the three solutions. The GPS-based solution (left) is nearly identical to the GPS, InSAR and AZO-based solution (center). The GPS, InSAR and MAI-based solution (right) is slightly different from them, suggesting the largest slip concentration was skewed southward (see text). Color scale is in meters.

the AZO displacements with the more precise MAI data. This solution provides a 1 cm improvement in MAI data prediction and a 0.2 cm improvement in InSAR data fitting. The solution (Figure 5-13, right panel) is skewed southward with respect to the previous solutions. This is in accordance with spatial improvement in data fitting near the southern end of the fault (Figures 5-7 and 5-12, also 5-6 and 5-11). We note that the area south of the fault is lacking in GPS sites, and contains along-track displacements that are too small for the AZO precision. As a result, the MAI technique provides the only information available about deformation in that area.

We compare the shallow-most section of our fault slip distributions to independent field observations of the earthquake surface rupture by USGS Scientists [1999] in Figure 5-14. The GPS and GPS, InSAR and AZO-based solutions provide two similar surface rupture patterns (green and blue curves in Figure 5-14, respectively), with the GPS, InSAR and AZO-based solution providing a slightly different curve. We note that the scatter in the field data is in the order of half a meter and higher, which is considerably larger than the individual differences between the three model solutions.

We summarize that while AZO data, when weighted according to published precision, are too noisy to influence a solution that is already well-constrained by GPS displacements, MAI data do receive some weight in a similar inversion. While the MAI data do not overwhelm the GPS data, they provide additional information south of the fault and are precise enough to improve the spatial distribution of both slip and predicted GPS displacements.

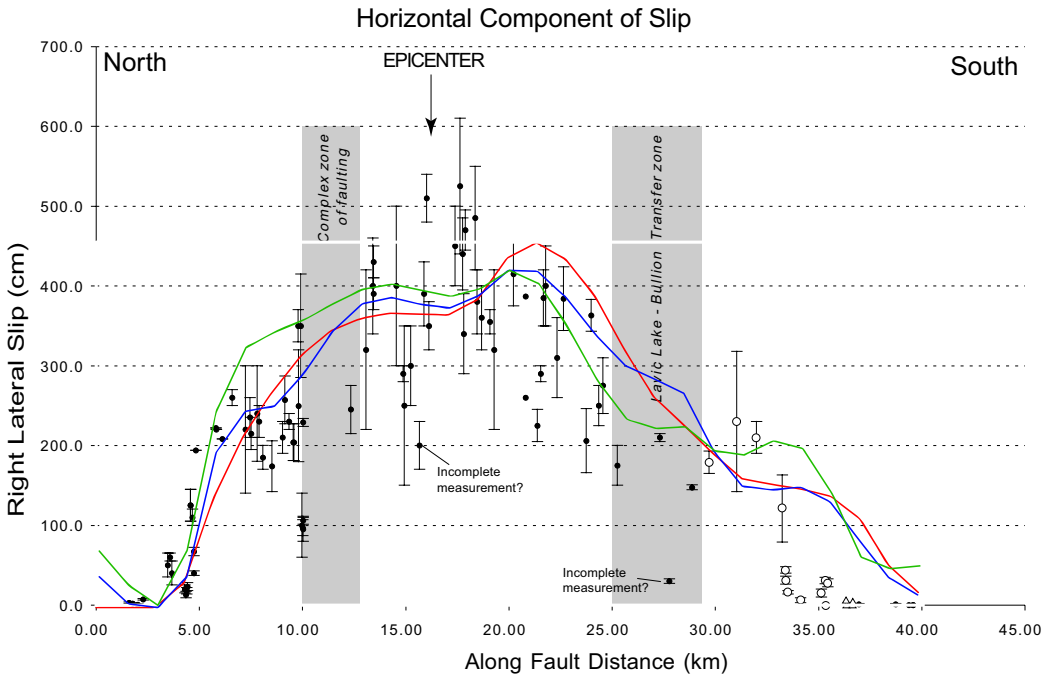

Figure 5-14: Comparison of model and field measurements for the surface rupture. Black dots and circles with error-bars represent the field measurements [*USGS Scientists*, 1999]. The green curve represents GPS-based solution prediction of the surface rupture. Blue curve represents a similar prediction by the GPS, InSAR and AZO-based solution. Red curve represents the GPS, InSAR and MAI model prediction. The uncertainties in the field data imply that all three solutions fit the measurements equally (un)well.

Chapter 6

Thesis Findings and Conclusions

Satellite radar interferometry (InSAR) can be used to study the seismic cycle in regions that are inaccessible to ground-based geodetic methods. In this work we extended InSAR from one dimension to two dimensions, thereby increasing the range and scope of investigations possible with InSAR.

We find that InSAR raw data contain along-track phase information, which can be extracted by processing the data into forward- and backward-looking interferograms.

In this method, topographic and range phase contributions cancel out, as do some of the errors via subtraction of the phase of the forward- and backward-looking interferograms. The resulting phase can be mapped directly into along-track displacements. We call this method of extracting the along-track phase contribution multiple aperture InSAR (MAI).

We calculate the expected precision of the new method, based on published theoretical calculations of InSAR precision [*Rodriguez and Martin*, 1992; *Zebker and Villasenor*, 1992]. The predicted precision varies from 3 to 11 centimeters, a factor of 2 and more improvement compared to the previously available pixel-offset calculations. This estimate takes into account the cruder resolution of the forward- and backward-looking interferograms, and a range of expected SNR and interferometric correlation values.

We note that MAI's predicted precision depends on the amount of beam steering in the forward- and backward-looking interferograms. The optimal steering can be calculated from the conventional InSAR SNR and correlation.

We applied MAI to InSAR data of the 1999, California Hector Mine earthquake. We tested the method's precision by comparing the results to pixel-offset [*Fialko et al.*, 2001] and GPS displacements [*Agnew et al.*, 2002] for the same event. The MAI results agree qualitatively with pixel-offsets, and show the deformation over a wider extent. We compare MAI and GPS displacements by projecting the GPS displacements in the along-track direction. The GPS data were collected at different times after the earthquake, from a few days to several months so that some post-earthquake deformation must be accounted for. The root mean square error (rmse) of the MAI-GPS difference varies from 5 to 6.9 centimeters, for GPS data that were collected up to two weeks and up to two months after the earthquake, respectively.

We also compared the predicted precision to the actual precision, by comparing the MAI-GPS difference in the GPS site locations with the predicted errors for these locations. We found that for 84% of the sites, MAI's actual precision betters or equals the predicted precision. We note that the predicted precision for the GPS site locations varied from 5 to 24 centimeters. This allowed us to test MAI's precision only on this range.

We published these findings in the journal *Geophysics Research Letters* [*Bechor and Zebker*, 2006] and in two scientific meetings. We note that MAI can be easily implemented with no code changes using conventional InSAR software packages.

We also investigated the improvement in models of the Hector Mine earthquake coseismic slip distribution with the use of the new data. We found that the main features of the slip distribution are revealed by using the GPS displacements alone. In this scenario, the AZO displacements with their published errors do not have enough weight to influence a combined GPS-AZO inversion, as the $\sim$ 15 cm AZO-GPS disagreement tends to enter the AZO error budget in the solution. The MAI displacements, on the other hand, are precise enough to modify the solution, however their weight in the solution is lower than that of the GPS data.

Bibliography

[1] Agnew, D. C, S. Owen, Z. K. Shen, G. Anderson, J. Svarc, H. Johnson, K. E. Austin and R. Reilinger (2002), Stress field variations in the Swiss Alps and the northern Alpine foreland derived from inversion of fault plane solutions, *Bull. Seismo. Soc. Am., 92*, 4, 1355–1364.

[2] Arnadottir, T., S. Jonsson, R. Pederspn and G. B. Gudmundsson (2003), Coulomb stress changes in the South Iceland Seismic Zone due to two large earthquakes in June 2000, *Geophys. Res. Lett., 30*, (5), 1205, doi:10.1029/2002GL016495.

[3] Bamler, R. and P. Hartl (1998), Synthetic aperture radar interferometry, *Inverse Problems 14*, R1-R54 doi:10.1088/0266-5611/14/4/001.

[4] Bechor, B. D. N. and H. A. Zebker (2006), Measuring two-dimensional movements using a single InSAR pair, *Geophys. Res. Lett., 33*, L16311, doi:10.1029/2006GL026883.

[5] Burgmann, R., G. Hilley, A. Ferretti, F. Novali (2006), Resolving vertical tectonics in the San Francisco Bay Area from permanent scatterer InSAR and GPS analysis, *Geology, 34*, (3), 221–224, doi: 10.1130/G22064.1.

[6] Cakir, Z., A. M. Akoglu, S. Belabbes, S. Ergintav and M. Meghraoui (2005), Creeping along the Ismetpasa section of the North Anatolian fault (Western Turkey): Rate and extent from InSAR, *Earth and Plantary Sci. Lett., 238*, 225–234.

[7] Cakir, Z., M. Meghraoui, A. M. Akoglu, N. Jabour, S. Belabbes and L. Ait-Brahim (2006), Surface Deformation Associated with the Mw 6.4, 24 February 2004 Al

Hoceima, Morocco, Earthquake Deduced from InSAR: Implications for the Active Tectonics along North Africa, *Bull. SSA, 96*, (1), 59–68, doi:10.1785/0120050108.

[8] Catita, C., K. L. Feigl, J. Catalo, J. M. Miranda and L. M. Victor (2005), InSAR time series analysis of the 9 July 1998 Azores earthquake, *Int. J. of Rem. Sens., 26*, (13), 2715–2729, doi: 10.1080/01431160512331337835.

[9] Chen, C.W. and H. A. Zebker (2002), Phase unwrapping for large SAR interferograms: statistical segmentation and generalized network models, *IEEE Trans. Geoscience and Remote Sensing, 40*, (8), 1709–1719, doi: 10.1109/TGRS.2002.802453.

[10] Crippa, B., M. Crosetto, E. Biescas, C. Troise, F. Pingue and G. De Natale (2006), An advanced slip model for the Umbria-Marche earthquake sequence: coseismic displacements observed by SAR interferometry and model inversion, *Geophys. J. Int., 164*, (1), 36, doi:10.1111/j.1365-246X.2005.02830.x.

[11] Du, Y., A. Aydin and P. Segall (1992), Comparison of various inversion techniques as applied to the determination of a geophysical deformation model for the 1983 Borah Peak earthquake, *Bull. SSA, 82*, (4), 1840–1866.

[12] Eldhuset, K., P. H. Andersen , S. Hauge, E. Isaksson, D. J. Weydahl (2003), ERS tandem InSAR processing for DEM generation, glacier motion estimation and coherence analysis on Svalbard, *Int. J. of Remote Sensing, 24*, (7), 1415–1437.

[13] Ferretti, A., C. Prati, F. Rocca, Permanent scatterers in SAR interferometry, *IEEE Trans. Geoscience and Remote Sensing, 39*, (1), 8–20.

[14] Fialko, Y., M. Simons and D. Agnew (2001), The complete (3-D) surface displacement field in the epicentral area of the 1999 Mw 7.1 Hector Mine earthquake, California, from space geodetic observations, *Geophys. Res. Lett., 28*, 16, 3063–3066.

[15] Fialko, Y., (2004), Probing the mechanical properties of a seismically active crust with space geodesy: Study of hte coseismic deformation due to the

1992 Mw7.3 Landers (southern California) earthquake, *Geophys. Res. Lett., 109*, B03307, DOI:10.1029/2003JB002756.

[16] Fialko, Y., D. Sandwell, M. Simons and P. Rosen (2005), Three dimensional deformation caused by the Bam, Iran, earthquake and the origin of the shallow slip deficit, *Nature, 435*, 295-299, doi:10.1038/nature03425.

[17] Fialko, Y. (2006), Interseismic strain accumulation and the earthquake potential on the southern San Andreas fault system, *Nature, 441*, (7096), 968–971.

[18] Fielding, E., M. Talebian, P. A. Rosen, H. Nazari, J. A. Jackson, M. Ghorashi, and R. Walker, (2005), Surface ruptures and building damage of the 2003 Bam, Iran, earthquake mapped by satellite synthetic aperture radar interferometric correlation, *J. Geophys. Res., 110*, (B03302), doi:10.1029/2004JB003299.

[19] Forster, R.R., K. C. Jezek, L. Koenig, E. Deeb (2003), Measurement of glacier geophysical properties from InSAR wrapped phase, *IEEE Trans. Geosci. Remote Sens., 41*, (11), 1, 2595–2604.

[20] Froger, J. L., Y. Fukushimana, P. Briole, T. Staudachr, T. Souriot and N. Villneuve (2004), The deformation field of the August 2003 eruption at Piton de la Fournaise, Reuinon Island, mapped by ASAR interferometry, *J. Geophys. Res, 31*, L14601, doi:10.1029/2004GL020479.

[21] Funning, G. J., B. P. Parsons, T. J. Wright, J. A. Jackson and E. J. Fielding (2005), Surface displacements and source parameters of the 2003 Bam (Iran) earthquake from Envisat advanced synethetic aperture radar imagery, *J. Geophys. Res., 110*, B09406, doi:10.1029/2004JB003338.

[22] Funning, G. J., R¿ M. D. Barke, S. H. Lamb, E. Minaya, B. Parsons and T. J. Wright (2005), The 1998 Aiquile, Bolivia earthquake: A seismically active fault revealed with InSAR, *Earth and Planetary Sci. Lett., in press*

[23] Gabriel, A. K., R. M. Goldstein and H. A. Zebker (1989), Mapping small evaluation changes over large areas: Differential radar interferometry, *J. Geophys. Res., 94*, (B7), 9183–9191.

[24] Goldsten, R. M. and H. A. Zebker, Interferometric radar measurement of ocean surface currents (1987), *Nature, 328*, (6132), 707–709.

[25] Gray, A. L., K. E. Mattar, P. W. Vachon, R. Bindschadler, Jezek K.C., R. Forster, and J. P. Crawford (1998), InSAR results from the RADARSAT Antarctic Mapping Mission data:estimation of glacier motion using a simple registration procedure, *IGARSS Proceedings, IEEE Int., 3*, 1638–1640.

[26] Hilley, G. E., R. Burgmann, A. Ferretti, F. Novali and F. Rocca (2004), Dynamics of Slow-Moving Landslides from Permanent Scatterer Analysis, *Science, 34*, (5679), 1952–1955, DOI: 10.1126/science.1098821.

[27] Hooper, A., H. A. Zebker, P. Segall and B. Kampes, A new method for measuring deformation on volcanoes and other natural terrains using InSAR persistent scatterers (2004), *Geophys. Res. Lett., 31*, L23611, doi:10.1029/2004GL021737.

[28] Jacobs, A., D. Sandwell, Y. Fialko and L. Sichoix (2002), The 1999 (Mw 7.1) Hector Mine, California, Earthquake: Near-Field Postseismic Deformation from ERS Interferometry, Bull. SSA, 92, (4), 1433–1442, doi:10.1785/0120000908.

[29] Jonsson, S. Zebker, H. Segall and P. Amelung, F. (2002), Fault Slip Distribution of the M w 7.1 Hector Mine, California, Earthquake, Estimated from Satellite Radar and GPS Measurements, *Bull. Seismo. Soc. Am., 92*, 4, 1377–1389.

[30] Joughin, I. R., R. Kwok and M. A. Fahnestock (1998), Interferometric estimation of three-dimensional ice-flow using ascnding and descnding passs, *IEEE Trans. Geosci. Remote Sens., 36*, 1, 25-37.

[31] Langbein, J., R. Borcherdt, D. Dreger, J. Fletcher, J. L. Hardebeck, M. Hellweg, C. Ji, J. Johnston, J. R. Murray, R. Nadeau, M. J. Rymer, and J. A. treiman, Preliminary Report on the 28 September 2004, M 6. 0 Parkfield, California Earthquake (2005), *Seism. Res. Lett., 76*, (1) 10-26.

[32] Lawson, C. L. and R. J. Hanson (1974), Solving Least Squares Problems, Englewood Cliffs, N.J., Prentice-Hall.

[33] Lyons, S. and D. Sandwell (2003), Fault creep along the southern San Andreas from interferometric synthetic aperture radar, permanent scatterers, and stacking, *J. Geophys. Res, 108*, B1, 2047, doi:10.1029/2002JB001831.

[34] Massonnet, D., M. Rossi, C. Carmona, F. Adragna, G. Peltzer, K. Feigl, T. Rabaute, (1993), The displacement field of the Landers earthquake mapped by radar interferometry, *Nature, 364*, 138–142.

[35] Michel, R., J. P. Avouac and J. Taboury (1999), Measuring ground displacements from SAR amplitude images: application to the Landers earthquake, *Geophys. Res. Lett., 26*(7), 875–878.

[36] Michel, R., J. P. Avouac and J. Taboury (1999), Measuring near field coseismic displacements from SAR images: application to the Landers earthquake, *Geophys. Res. Lett., 26*(19), 3017–3020.

[37] Murray, J. R., P. Segall, P. Cervelli, P. Prescott, W. Svarc (2001), Inversion of GPS data for spatially variable slip-rate on the San Andreas Fault near Parkfield, CA, *Geophys. Res. Lett., 28*, (2), 359–362.

[38] Peltzer, G. and P. Rosen (1995), Surface Displacement of the 17 May 1993 Eureka Valley, California, Earthquake Observed by SAR Interferometry, *Science, 268*, (5215), 1333–1336, doi:10.1126/science.268.5215.1333.

[39] Peltzer, G., P. Rosen, F. Rogez and K. Hudnut (1996), Postseismic Rebound in Fault Step-Overs Caused by Pore Fluid Flow, *Science, 273*, (5279), 1202–1204, doi:10.1126/science.273.5279.1202.

[40] Peltzer, G., P. Rosen, F. Rogez and K. Hudnut (1998), Poroelastic rebound along the Landers 1992 earthquake surface rupture, *J. Geophys. Res., 103*, (B12), 30,131–30,146.

[41] Peltzer, G., F. Crampe and G. King (1999), Evidence of Nonlinear Elasticity of the Crust from the Mw7.6 Manyi (Tibet) Earthquake, *Science, 286*, 272-276.

[42] Peltzer, G., F. Crampe, S. Hansley and P. Rosen (2001), Transient strain accumulation and fault interaction in the Eastern California shear zone, *Geology, 29*, (11), 75–978, doi:10.1130/0091-7613(2001)029¡0975:TSAAFI¿2.0.CO.

[43] Price, E. J. and R. Burgmann (2002), Interactions between the Landers and Hector Mine, California, Earthquakes from Space Geodesy, Boundary Element Modeling, and Time-Dependent Friction, *Bull. SSA, 92*, 4, 1450–1469, doi:10.1785/0120000924.

[44] Pritchard, M. E., M. Simons, P. A. Rosen, S. Hensley and F. H. Webb (2002), Co-seismic slip from the 1995 July 30 Mw= 8.1 Antofagasta, Chile, earthquake as constrained by InSAR and GPS observations, *Geophys. J. Int., 150*, (2), 362, doi:10.1046/j.1365-246X.2002.01661.x.

[45] Richman, D. (1971), Three dimensional azimuth-correcting mapping radar, *United Technologies Corporation, USA*.

[46] Rodriguez, E., and J. M. Martin (1992), Theory and design of interferometric synthetic aperture radars, *IEEE PROCEEDINGS-F, 139*, (2), 149-159.

[47] Sandwell, D. T., L. Sichoix and B. Smith (2002), The 1999 Hector Mine Earthquake, Southern California: Vector Near-Field Displacements from ERS InSAR, *Bull. SSA, 92*, (4), 1341–1345, doi:10.1785/0120000901.

[48] Simons, M., Y. Fialko and L. Rivra (2002), Co-sismic deformation from the 1999 Mw 7.1 Hector Mine, California, earthquake as inferred from InSAR and GPS observations, *Bull. SSA, 92*, (4),1390-1402.

[49] Wadge, G., B. Parsons and the Evinsar science team (2003), Achieving the EVINSAR Objectives with TerraSAR-L, in *Proc. FRINGE 2003 Workshop (ESA SP-550). 1-5 December 2003, ESA/ESRIN, Frascati, Italy.* Editor: H. Lacoste. Published on CDROM., p.41.1.

[50] Wald, J. D., D. V. Helmberger and T. H. Heaton (1991), Rupture model of the 1989 Loma Prieta earthquake from the inversion of strong-motion and broadband teleseismic data, *Bull. SSA, 81*, (5), 1540-1572.

[51] Wright, T. J., Z. Lu and C. Wicks (2003), Source model for the Mw 6.7, 23 October 2002, Nenana Mountain Earthquake (Alaska) from InSAR, *Geophys. Res. Lett., 34*, (18), 1974, doi:10.1029/2003GL018014.

[52] Wright, T. J., Z. Lu and W. Wicks (2004), Constraining the Slip Distribution and Fault Geometry of the Mw 7.9, 3 November 2002, Denali Fault Earthquake with Interferometric Synthetic Aperture Radar and Global Positioning System Data, *Bull. SSA, 94*, 6B, S175–S189.

[53] Wright, T. J., B. E. Parsons, and Z. Lu (2004), Toward mapping surface deformation in three dimensions using InSAR , *Geophys. Res. Lett., 31*, (1), 1, L01607, doi 10.1029/2003GL018827.

[54] Wright, T. J., B. E. Parsons, P. C. England and E. Fielding (2004), InSAR Observations of Low Slip Rates on the Major Faults of Western Tibet, *Science, 305*, (5681), 236–239, doi: 10.1126/science.1096388.

[55] Zebker, H. A. and R. M. Goldsten, Topographic mapping from interferometer synthetic aperture radar observations (1986), *J. Geophys. Res., 91*, (B5), 4993–5000.

[56] Zebker, H. A., and J. Villasenor (1992), Decorrelation in interferomtric radar echos, *IEEE Trans. Geosci. Remote Sens., 30*, 950-959.

[57] Zebker, H. A., C. L. Werner, P. Rosen, S. Hensley (1994), Accuracy of Topographic Maps Derived from ERS-1 Interferometric Radar, *IEEE Trans. Geosci. Remote Sens., 32*, (4), 823.